Journal of Nanobiotechnology

RESEARCH

Open Access

Oxygen vacancy-engineered cerium oxide mediated by copper-platinum exhibit enhanced SOD/CAT-mimicking activities to regulate the microenvironment for osteoarthritis therapy

Junxu Yang[1,3†], Shihui Xiao[1,3†], Jiejia Deng[1,2†], Yuquan Li[1,5], Hao Hu[1], Jiawei Wang[1], Chun Lu[4], Guanhua Li[1,3], Li Zheng[1*], Qingjun Wei[1,5*] and Jingping Zhong[1*]

Abstract

Cerium oxide (CeO_2) nanospheres have limited enzymatic activity that hinders further application in catalytic therapy, but they have an "oxidation switch" to enhance their catalytic activity by increasing oxygen vacancies. In this study, according to the defect-engineering strategy, we developed $PtCuO_X/CeO_{2-X}$ nanozymes as highly efficient SOD/CAT mimics by introducing bimetallic copper (Cu) and platinum (Pt) into CeO_2 nanospheres to enhance the oxygen vacancies, in an attempt to combine near-infrared (NIR) irradiation to regulate microenvironment for osteoarthritis (OA) therapy. As expected, the Cu and Pt increased the Ce^{3+}/Ce^{4+} ratio of CeO_2 to significantly enhance the oxygen vacancies, and simultaneously CeO_2 (111) facilitated the uniform dispersion of Cu and Pt. The strong metal-carrier interaction synergy endowed the $PtCuO_X/CeO_{2-X}$ nanozymes with highly efficient SOD/CAT-like activity by the decreased formation energy of oxygen vacancy, promoted electron transfer, the increased adsorption energy of intermediates, and the decreased reaction activation energy. Besides, the nanozymes have excellent photothermal conversion efficiency (55.41%). Further, the $PtCuO_X/CeO_{2-X}$ antioxidant system effectively scavenged intracellular ROS and RNS, protected mitochondrial function, and inhibited the inflammatory factors, thus reducing chondrocyte apoptosis. In vivo, experiments demonstrated the biosafety of $PtCuO_X/CeO_{2-X}$ and its potent effect on OA suppression. In particular, NIR radiation further enhanced the effects. Mechanistically, $PtCuO_X/CeO_{2-X}$ nanozymes reduced ras-related C3 botulinum toxin substrate 1 (Rac-1) and *p*-p65 protein expression, as well as ROS levels to remodel the inflammatory microenvironment by inhibiting the ROS/Rac-1/nuclear factor kappa-B (NF-κB) signaling pathway. This study introduces new clinical concepts and perspectives that can be applied to inflammatory diseases.

Keywords Nanozymes, Oxygen vacancies, Enzyme catalytic activity, Anti-inflammatory, Osteoarthritis

†Junxu Yang, Shihui Xiao and Jiejia Deng have contributed equally to this work.

*Correspondence:
Li Zheng
zhengli224@163.com
Qingjun Wei
weiqingjungxnn@163.com
Jingping Zhong
jingpingzhong@163.com
Full list of author information is available at the end of the article

Graphical Abstract

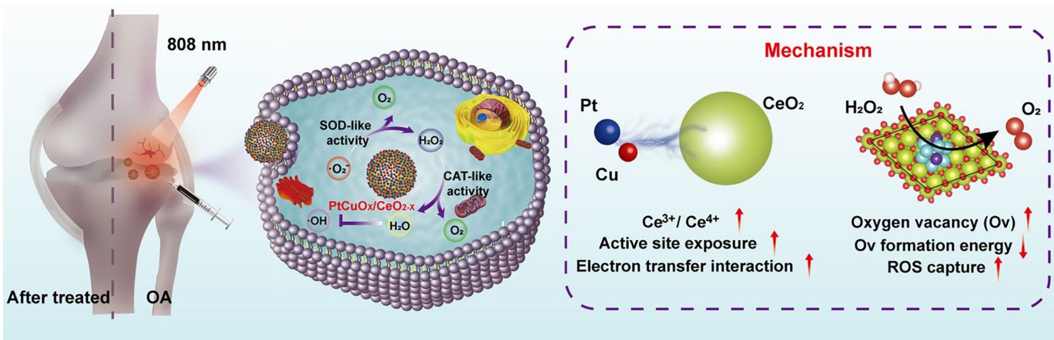

Introduction

Osteoarthritis (OA) is a destructive inflammatory articular cartilage disease affecting 528 million people worldwide [1]. Currently, there are no effective therapeutic drugs for OA, and joint replacement surgery can only be performed in the late stages of the disease, which causes tremendous pain to patients [2, 3]. Therefore, there is an urgent need to develop new treatment strategies for OA. According to research, excessive reactive oxygen species (ROS) and reactive nitrogen species (RNS) and their activated nuclear factor kappa-B (NF-κB) signaling pathway, leading to oxidative stress, were closely related to the pathogenesis of OA [4–6]. Therefore, an effective means of treating OA involves scavenging the overproduced ROS and RNS, such as superoxide anion ($\cdot O_2^-$), hydroxyl radical (·OH), hydrogen peroxide (H_2O_2), and nitric oxide (·NO)7. Natural catalase (CAT) and superoxide dismutase (SOD) are the antioxidant defense systems in the body, but in the OA, excessive ROS and RNS disrupt the balance of the redox system [8]. Direct supplementation of natural SOD and CAT has limitations, including complex synthesis and purification processes [9], poor thermal stability [10], and short shelf life [11]. Therefore, researchers aim to design efficient artificial enzymes that mimic the catalytic activity of natural enzymes.

Nanozymes offer significant advantages, such as high enzyme-like activity [12], good stability [13], low cost [14], and controllable synthesis, which have attracted wide attention and recognition. Among them, cerium oxide (CeO_2) was well known to exhibit various enzyme-mimetic properties for the treatment of inflammatory diseases, such as SOD and CAT, which was achieved by modulating the electronic structure through reversible Ce^{3+} (reduction) and Ce^{4+} (oxidation) transitions [15]. For example, Gao et al. [16] used hyaluronic acid/serotonin-modified CeO_2 nanomedicine to mimic SOD/CAT-like activities for scavenging ROS, thereby removing inflammatory factors and facilitating intestinal epithelial barrier repair for ulcerative colitis therapy. Lin et al. [17] used hyaluronic acid-loaded CeO_2 as a ROS scavenger that protected chondrocytes from IL-1β-induced oxidative stress damage for OA therapy. Although CeO_2-based nanozymes show promising therapeutic potential for inflammatory diseases, they still face challenges, including low enzyme activity, high toxicity, and easy aggregation [18–20].

Excitingly, the doping of copper (Cu) nanospheres on CeO_2 can improve the ratio of the Ce^{3+}/Ce^{4+} in CeO_2 to significantly increase the occupancy of oxygen vacancies and expose more active sites, thus further enhancing its catalytic activity. For example, Guo et al. [21] demonstrated that doping Cu in CeO_2 weakened the Ce–O bonds, which facilitated the generation of oxygen vacancy active sites, and the synergistic interactions enhanced the catalytic activity for CO_2 reduction. In addition, Zhang et al. [22] demonstrated that Cu/CeO_2 had higher adsorption energy for reactants than noble metals (such as Pd and Au), making it more favorable for H_2 dissociation reactions. However, the development of Cu-loaded CeO_2 nanospheres to mimic the activities of natural SOD/CAT enzymes has rarely been reported, possibly because Cu^{1+} has more catalytic activity than Cu^{2+}, but Cu^{1+} is unstable, resulting in insufficient catalytic activity and stability [23]. Fortunately, introducing platinum (Pt) into Cu can stabilize the Cu^{1+}, synergistically enhancing CO oxidation [24]. And Zou et al. [25] demonstrated that the addition of Pt changed the charge state of the Cu surface, and Cu also modulated the d-band center of Pt, thus optimizing the catalytic performance of CO_2 reduction. In addition, photothermal therapy has been shown to enhance the enzymatic activity of nanozymes, thereby improving the therapeutic effect [26]. Therefore, we expected that

Cu/Pt co-loaded CeO_2 could enhance the photothermal effect under near-infrared (NIR) irradiation and further optimize the catalytic activity of SOD/CAT-like enzymes, thus providing a synergistic therapy for OA, which has not been reported in the literature.

Here, a "defect engineering construction strategy" [27] was employed to develop $PtCuO_X/CeO_{2-X}$ nanozymes as highly efficient SOD/CAT mimics by introducing bimetallic Cu and Pt into CeO_2 microspheres to enhance the oxygen vacancies, in an attempt to combine NIR irradiation to regulate microenvironment for OA therapy. As expected, the Cu and Pt increased the Ce^{3+}/Ce^{4+} ratio of CeO_2 to significantly enhance the oxygen vacancies, and simultaneously CeO_2 (111) facilitated the uniform dispersion of Cu and Pt. The strong metal-carrier interaction synergy endowed the $PtCuO_X/CeO_{2-X}$ nanozymes with highly efficient SOD/CAT-like activity by the decreased formation energy of oxygen vacancy, promoted electron transfer, the increased adsorption energy of intermediates, and the decreased reaction activation energy. Besides, the nanozymes have excellent photothermal conversion efficiency (55.41%). In vitro experiments demonstrated that the $PtCuO_X/CeO_{2-X}$ SOD/CAT antioxidant system effectively eliminated ROS and RNS, restored mitochondrial function, and inhibited the inflammatory factors, leading to a reduction in chondrocyte apoptosis. In vivo experiments demonstrated the biosafety of $PtCuO_X/CeO_{2-X}$ and the potent effect on OA progression. In particular, NIR radiation further enhanced the effects. Mechanistically, $PtCuO_X/CeO_{2-X}$ nanozymes reduced ras-related C3 botulinum toxin substrate 1(Rac-1) and *p*-p65 protein expression, as well as ROS levels to remodel the inflammatory microenvironment by inhibiting the ROS/Rac-1/NF-κB signaling pathway (Fig. 1).

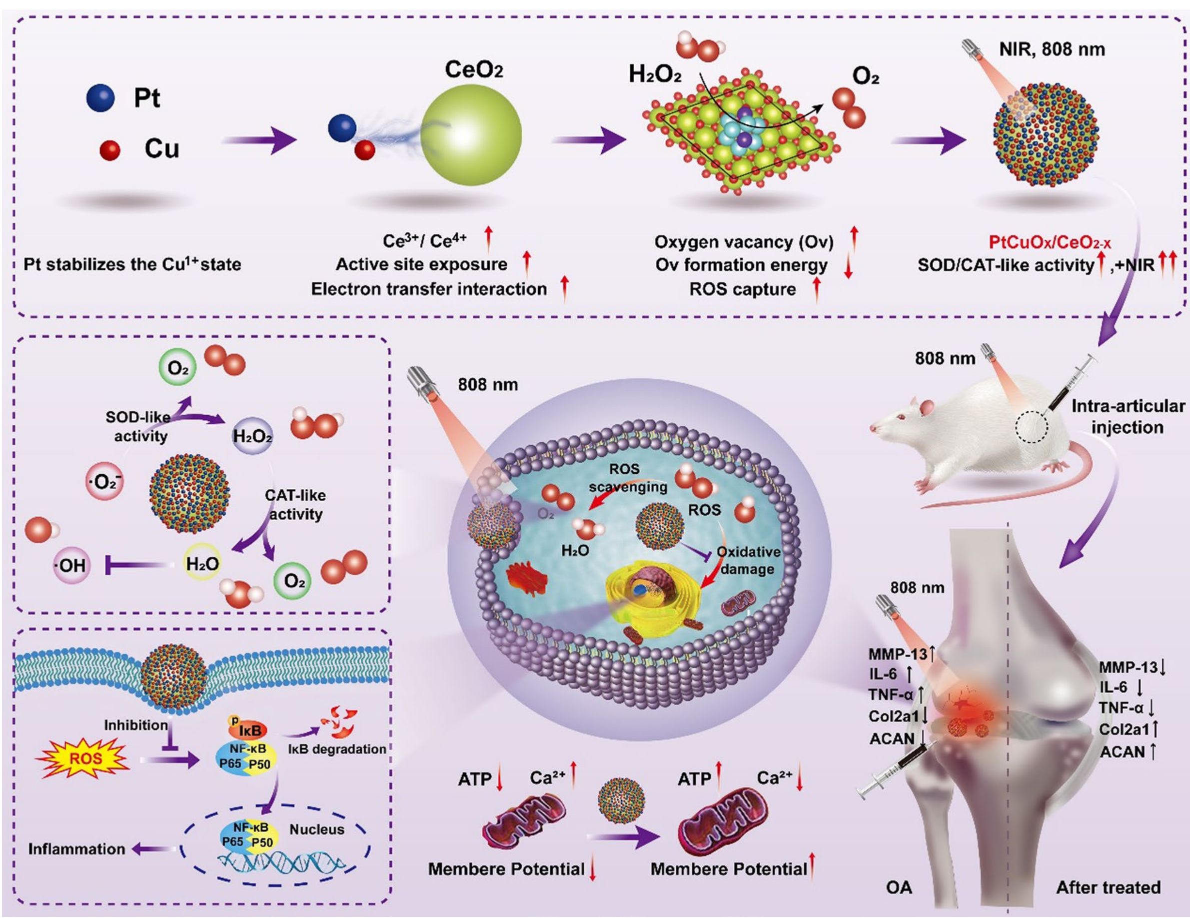

Fig. 1 $PtCuO_X/CeO_{2-X}$ nanozymes scavenge ROS in chondrocytes, improve mitochondrial function, and treat OA. CuPt-loaded nanospheres loaded increased the Ce^{3+}/Ce^{4+} ratio, accelerated the electron transfer, sufficiently exposed the active sites, increased the oxygen vacancy content and the free radicals adsorption energy, and lowered the activation energy barriers to enhance SOD/CAT-like activity. $PtCuO_X/CeO_{2-X}$ nanozymes remodel the inflammatory microenvironment by inhibiting the ROS/Rac-1/NF-κB pathway

Materials and methods

Methods for synthesis and characterization of nanozymes

Materials

Cerium nitrate hexahydrate ($CeN_3O_9·6H_2O$, 99.5%) was purchased from Macklin Company in China. Hydrazine hydrate ($N_2H_4·H_2O$, AR) and copper sulfate ($CuSO_4·5H_2O$, AR) were purchased from Chengdu Jinshan Chemical Reagent Co. Anhydrous ethanol was purchased from China National Pharmaceutical Chemical Reagent Co. Platinum tetrachloride ($PtCl_4$) and ethylene glycol ($C_2H_4O_2$, > 99%) were purchased from Macklin Company in China. All chemicals were used directly without further purification.

Synthesis of CeO_2

The nanoparticles were synthesized based on previous research [28–30]. $Ce(NO_3)_3·6H_2O$ (4.6 mmol/L) was dissolved in 2 mL of deionized water, followed by the addition of acetic acid (2 mL) and ethylene glycol (52 mL). The solution was transferred to a Teflon liner, maintained at 180 °C for 200 min, centrifuged and dried to obtain the product, and calcined in air at 400 °C for 4 h to obtain CeO_2 nanospheres.

Synthesis of $PtCuO_X/CeO_{2-X}$

$CuSO_4$ (50 mg) and CeO_2 (100 mg) were dissolved in deionized water (4 mL), respectively, added to 80 mL of anhydrous ethanol, and hydrazine hydrate was added dropwise and reacted for 2 h to give the intermediate product, CuO_X/CeO_{2-X}. Similarly, $PtCl_4$ (20 mg) and CuO_X/CeO_{2-X} (100 mg) were dissolved in deionized water (4 mL) in the same manner as above. $PtCuO_X/CeO_{2-X}$ nanospheres were obtained.

Characterization methods

Transmission electron microscopy (TEM) and energy dispersive spectroscopy (EDS) (FEI Talos f200s, FEI, USA) were used to determine the morphology, size, and composition of the nanospheres. Dynamic light scattering (DLS) (Zetasizer Nano ZS ZEN3600, Malvern, UK) was used for hydrodynamic diameters of nanospheres, and X-ray photoelectron spectroscopy (XPS) (Thermo Fisher ESCALAB 250Xi, USA) was used for structure–activity relationships of nanospheres. An X-ray diffractometer (Rigaku, Ultima IV, Japan) was used for the crystallinity of nanospheres. An inductively coupled plasma mass spectrometer (Thermo iCAP 6300 Duo, USA) was used for the determination of elemental content, and the JEOL JES FA200 ESR spectrometer was used for the evaluation of free radical scavenging capacity. Fourier transform infrared spectrometer (IRAffinity-1S, Shimadzu, Japan) was used for infrared absorption.

DFT computational details

All DFT calculations were carried out using the Vienna ab initio simulation package (VASP) [31]. The Perdew-Burke-Ernzerhof (PBE) [32] functional was used to treat the exchange–correlation interactions. The plane wave basis set with a kinetic energy cutoff of 400 eV and the energy convergence criterion of 10^{-4} eV was used for structure relaxation. All surface calculations used a (1 × 1 × 1) Monkhorst–Pack k-point sampling. H_2O, H_2O_2, and O_2 were calculated in boxes of 15Å × 15Å × 15Å, with the gamma point only.

The adsorption energy (E_{ads}) is calculated as follows:

$$E_{ads} = E_{(adsorbates + catalysts)} - E_{adsorbates} - E_{catalysts}$$

$E_{(adsorbates + catalysts)}$, $E_{adsorbates}$, and $E_{catalysts}$ are the energy of the whole system, adsorbates, and catalysts, respectively.

Photothermal performance testing

Photothermal heating curve

CeO_2 and $PtCuO_X/CeO_{2-X}$ solutions (1 mL, 50 μg/mL) were placed in Eppendorf tubes, respectively. The samples were irradiated with an 808 nm laser (RAL808T1, Quartz Laser, China) for 15 min. Temperature changes were recorded and thermographic photographs were taken.

Photothermal conversion efficiency of $PtCuO_X/CeO_{2-X}$

$PtCuO_X/CeO_{2-X}$ solution (1 mL, 50 μg/mL) was irradiated with an 808 nm laser for 900 s. The laser was then turned off and allowed to cool naturally. The photothermal conversion efficiency (η) of the $PtCuO_X/CeO_{2-X}$ nanospheres was then calculated using Eqs. (1)-(4).

$$\Delta T_{max} = T_{max} - T_{surr} \tag{1}$$

$$\eta = (h\,A * \Delta T_{max} - Qs) / (I * (1 - 10 - A\lambda)) \tag{2}$$

$$\tau s = M_D * C_D / h\,A \tag{3}$$

$$\theta = (\Delta T) / (\Delta T_{max}) \tag{4}$$

(where "η" is the photothermal conversion coefficient, "h" is the heat transfer coefficient, "A" is the surface area of the vessel, and "h A" can be determined by a linear relationship between time and the negative logarithm of the cooling cycle (-lnθ). "T_{max}" is the equilibrium temperature, "T_{surr}" is the ambient temperature, "Qs" is the heat generation of the solvent, "I" is the irradiated laser power, "Aλ" is the absorbance of the $PtCuO_X/CeO_{2-X}$ nanospheres at 808 nm, "τs" is the time, "M_D" is the mass of the solvent, "C_D" is the heat capacity of the solvent, "θ" is the cooling cycle, and "ΔT" is the temperature difference during a given period).

The calculation procedure is as follows:

$\triangle T_{max} = T_{max}\text{-}T_{surr} = 48.1–25 = 23.1℃$

$hA = M_D * C_D / τs = 4.2*1/335.2 = 0.01252$.

$Qs = M_D * C_D (T_{PBS}\text{-}T_{surr}) = 4.2*0.001*(28.2–25) = 0.0013$.

$η = (hA\triangle T_{max}\text{-}Qs) /(I(1–10\text{-} Aλ)) = (0.0125*23.1–0.0013) /π*0.52*(1–10\text{-}0.47) = 0.5541$.

Photothermal stability

$PtCuO_X/CeO_{2-X}$ was dissolved in PBS (50 μg/mL) and irradiated with NIR light for 15 min before stopping the irradiation and allowing it to cool to room temperature before starting the next round of irradiation. This was repeated four times and the temperature changes were recorded to evaluate the photothermal stability.

Stability experiments of nanospheres

The dispersion of $PtCuO_X/CeO_{2-X}$ was recorded over 7 days and in different solvents. In addition, the average particle size and the polydispersity index (PDI) of the nanospheres in different solvents were measured by dynamic light scattering.

Enzyme mimetic properties of nanospheres

H_2O_2 decomposition test

We investigated the decomposition of H_2O_2 by $PtCuO_X/CeO_{2-X}$. Briefly, H_2O_2 solution (5 μL, 10 mM) was added to $PtCuO_X/CeO_{2-X}$ aqueous solution (5 mL, 50 μg/mL). The amount of oxygen released was quantified using a portable dissolved oxygen meter. The ability of the $PtCuO_X/CeO_{2-X}$ to continuously decompose H_2O_2 in vitro and in vivo was evaluated by adding H_2O_2 solution at the same time intervals using water and synovial fluid from OA rats, respectively, as the reaction system and the amount of oxygen released was recorded for four consecutive times.

ESR for ·OH detection

A solution of H_2O_2 derived from hydroxyl radicals was generated by full-band xenon irradiation for 5 min and scavenged with 5-tert-butylcarbonyl-5-methyl-1-pyrroline-N-oxide (BMPO, 10 mM). The scavenging ability of $PtCuO_X/CeO_{2-X}$ towards ·OH was evaluated by monitoring the changes in peak intensities compared to the control.

ESR for $\cdot O_2^-$ detection

In the ESR experiments, the $\cdot O_2^-$ was generated from KO_2 using 18-crown-6 as a stabilizer, while 5-(deoxy)-5-tert-butylcarbonyl-5-methyl-1-pyrroline-N-oxide (DMPO) was used as a scavenger. Peak intensities were measured for $PtCuO_X/CeO_{2-X}$ nanozymes and control materials.

$\cdot O_2^-$, H_2O_2, ·OH, and DPPH scavenging ability

The ability of CeO_2, $PtCuO_X/CeO_{2-X}$, and $PtCuO_X/CeO_{2-X}$ + NIR to scavenge $\cdot O_2^-$ was compared using a total superoxide dismutase assay kit (Beyotime, China). In addition, to verify whether the SOD-like activity of the nanozymes was concentration-dependent, the removal of $\cdot O_2^-$ by $PtCuO_X/CeO_{2-X}$ at concentrations of 20, 50, and 100 mg/mL was compared. The absorbance at 450 nm was measured using an enzyme-labeling device (Thermo Scientific, USA), and then the free radical scavenging rate was determined.

The scavenging activities of CeO_2, $PtCuO_X/CeO_{2-X}$, and $PtCuO_X/CeO_{2-X}$ + NIR against H_2O_2, ·OH, DPPH, and total ROS were compared using the catalase assay kit (Beyotime, China), the hydroxyl radical scavenging capacity assay kit (Solarbio, China), the DPPH radical scavenging capacity assay kit (Solarbio, China), and the total antioxidant capacity assay kit (Beyotime, China), respectively.

Primary chondrocyte harvest and culture

Sprague–Dawley (SD) rats were obtained from the Experimental Animal Center of Guangxi Medical University, and their articular cartilage was harvested and primary chondrocytes were extracted. The fresh cartilage tissue was minced, digested with trypsin for 30 min, centrifuged, resuspended with type II collagenase, and further digested for 4 h. Finally, cells were cultured in DMEM medium. Subsequent validation using third-generation anterior chondrocytes.

Cellular uptake assay

Grafting of fluorescent groups to nanospheres $PtCuO_X/CeO_{2-X}$ nanospheres (0.5 g) were added to a mixture of 3-aminopropyltrimethoxysilane (120 μL) and 95% ethanol (6 mL) and reacted for 1 h under light protection to obtain the intermediate containing amino-functionalized nanospheres. Dissolve 0.1 g of the above product in dimethylsulfoxide (400 μL), add Cy5-NHS ester (60 μL), then add dimethylsulfoxide until the volume reaches 800 μL, add 20 μL of triethylamine, and react for 24 h away from light.

Cellular uptake The chondrocytes (0.5×10^5 cells/well) were inoculated into 6-well plates, and after 24 h of culture, Cy5-$PtCuO_X/CeO_{2-X}$ nanospheres (50 μg/mL) were co-cultured with the cells, and the cells were fixed with 4% paraformaldehyde after 0.5, 6, and 12 h. The cytoskeleton was labeled with flavonoids and the nuclei were stained with DAPI. Confocal microscopy was performed to observe the uptake of nanospheres by cells.

Cell viability assay

Chondrocytes were cultured to attachment, co-cultured with the addition of nanospheres (30, 40, 50, 60, 70, and 80 μg/mL), and the cytotoxicity of nanozymes was evaluated by measuring the absorbance at 450 nm using a cell counting kit-8 (CCK-8, Biosharp, China) and a microplate reader (Molecular Devices, USA). In addition, the protective effect of nanozymes on inflammatory chondrocytes was evaluated. Briefly, chondrocytes were cultured to attachment, IL-1β was added, the culture was continued for 12 h, 50 μg/ml of nanozymes was added, and cell viability was determined after 24 h using a CCK-8 kit.

Observation of live and dead cell staining

Chondrocytes were cultured to adherence induced by the addition of IL-1β (10 ng/mL) for 12 h and then co-cultured with the addition of CeO_2, $PtCuO_X/CeO_{2-X}$, or $PtCuO_X/CeO_{2-X}$ + NIR (1.0 W/cm^2, 5 min) for 24 h. Cells were incubated with 1 μM calcein-AM and 1 μM propidium iodide (PI) for 30 min. Dead and live cells were then observed and recorded under a fluorescence microscope.

Measurement of ROS scavenging capacity in vitro

DCFH-DA Probe

ROS scavenging ability was detected using the fluorescent probe DCFH-DA (Beyotime, China). Chondrocytes (1×10^5 cells/well) were cultured until wall-adherent and induced by IL-1β for 12 h, then CeO_2, $PtCuO_X/CeO_{2-X,}$ and $PtCuO_X/CeO_{2-X}$ + NIR were added and cultured for 24 h, the probes were added, and the images were captured by fluorescence microscope (BD Biosciences, USA) after 30 min.

DAF-FM DA Probe

Nitric oxide (NO) levels in chondrocytes were detected using the Nitric Oxide Fluorescent Probe Assay Kit (Beyotime, China). Cells were treated in the same way as the image acquisition process described above.

DHE Probe

The level of intracellular superoxide ($\cdot O_2^-$) was detected with the fluorescent probe DHE (Beyotime, China). The chondrocytes were treated as described above. Fluorescence images of each group of chondrocytes after different treatments were captured by fluorescence microscope.

HPF probe

The intracellular hydroxyl radicals (·OH) levels were detected using the HPF fluorescent probe. Cells were treated in the same way as the image acquisition process described above.

[Ru (DPP)3]Cl2 (luminescent oxygen sensor)

The chondrocytes were treated as described above. Each group received an addition of [Ru(DPP)3]Cl2 (0.01 mg/mL, 10 μL), and fluorescence imaging was performed by fluorescence microscopy.

qRT-PCR

Chondrocytes (1×10^5 cells/well) were cultured to adherence, induced with IL-β for 12 h, and then co-cultured with CeO_2, $PtCuO_X/CeO_{2-X}$, and $PtCuO_X/CeO_{2-X}$ + NIR for 24 h. Total RNA was extracted with TRIZOL and cell lysis buffer, and cDNA was reverse transcribed with PrimeScript according to the instructions. qRT-PCR was performed by adding SYBR premix to the cDNA of the real-time PCR system (Thermo Fisher, USA), preincubating for 1 cycle at 95 °C for 600 s, followed by 45 cycles at 95 °C for 10 s, and amplifying at 60 °C for 60 s. The $2^{-\Delta\Delta Ct}$ method was used to quantify relative mRNA expression, normalized to GAPDH. The experiment was repeated in triplicate. Primer sequences are shown in Table 1.

Immunofluorescence of relevant inflammatory genes, chondroprotective genes, and apoptosis-related factors

Chondrocytes (1×10^5 cells/well) were cultured until apposition, induced by the addition of IL-1β for 12 h, and then co-cultured with the addition of CeO_2, $PtCuO_X/CeO_{2-X}$, and $PtCuO_X/CeO_{2-X}$ + NIR for 24 h. Cells were fixed with 4% paraformaldehyde solution (Biosharp, China) for 15 min, permeabilized with 3% H_2O_2 for 30 min, and blocked with goat serum for 30 min to

Table 1 Primer sequences used in qRT-PCR experiments

Gene name	Forward primer(5′-3′)	Reverse primer(5′-3′)
GAPDH	TCCAGTATGACTCTACCC ACG	CACGACATACTCAGCACCAG
MMP-13	ACCATCCTGTGACTCTTGCG	TTCACCCACATCAGGCATC
IL-6	ACAAGTCCGGAGAGGAGA CT	ACAGTGCATCATCGCTGTTC
TNF-α	GATCGGTCCCAACAAGGA GG	GCTTGGTGGTTTGCTACGAC
iNOS	GGTGAGGGGACTGGACTT TTAG	TCTCCGTGGGGCTTGTAGTT
ACAN	GAATGGGAGCCAGCCTAC AC	GAGAGGCAGAGGGAC TTTCG
Col2a1	GACTGTGCCTCGGAAGAA CT	TCTGGACGTTAGCGGTGTTG

detect non-specific antibodies. IL-6 (Affinity Biosciences, #DF6087), MMP-13(Proteintech Group,#18,165–1-AP), Col2a1(Affinity Biosciences,#AF0135), Bcl-2(Affinity Biosciences,#AF6139), Bax(Affinity Biosciences,#AF0120), Caspase-3(Affinity Biosciences,#AF6311) and β-actin(Affinity Biosciences,#AF7018) antibodies were incubated for 8–12 h, followed by FITC-conjugated anti-rabbit IgG (Boston, China) for 1 h. Finally, fluorescence images were captured with a fluorescence microscope (Olympus, Japan) and quantified using ImageJ software.

Mitochondrial membrane potential assay

JC-1 fluorescent staining

Cells were treated as described above, and after cells were incubated with JC-1 (Solarbio, China) working solution for 20 min, changes in JC-1 monomers and aggregates were recorded under a fluorescence microscope for each group, and fluorescence intensities were quantified using ImageJ software.

JC-1 flow cytometry

Cells were treated as described above. Cells in each treatment group were stained with a JC-1 fluorescent probe for 30 min, and the cells were washed three times with 4 °C PBS to precipitate. The intensity of red and green fluorescence signals were detected by flow cytometry (BD FACSCaliburTM Flow Cytometer).

Cytoplasmic Ca^{2+} concentration assay

Cell culture and treatment as described in Sect. "Immunofluorescence of relevant inflammatory genes, chondroprotective genes, and apoptosis-related factors", and at the end of the treatment, Fluo-4 AM (Beyotime, China) solution was co-incubated with chondrocytes for 30 min, and the fluorescence intensity of the cells was observed by fluorescence microscopy and finally quantitatively analyzed by fluorescence using ImageJ.

ATP measurement

Cell culture was performed as described above, and after 24 h, the cells were treated with IL-1β for 12 h. According to the Enhanced ATP Assay Kit (Beyotime, China) instructions, the cells of each group were completely lysed, and the standard curve was plotted first, after which the ATP content of each group was analyzed and calculated using a fluorescence microplate reader.

Apoptosis detection

Chondrocytes were cultured until apposition, then induced with IL-1β for 12 h. CeO_2, $PtCuO_X/CeO_{2-X}$, and $PtCuO_X/CeO_{2-X}$ + NIR were added to co-cultivate the cells for 24 h. Cells were then counted and 1.0×10^5 cells were collected, apoptosis detection reagents were added, and the cells were mixed and incubated away from light for 15 min, and the ratio of apoptosis was detected using Annexin V-APC /7-AAD Apoptosis Detection Kit (KeyGEN BioTECH, China) and flow cytometry (FCM) and analyzed by FlowJo_V10 software.

Immunoblotting assay for apoptosis-related proteins and ROS/Rac-1/NF-κB pathway proteins

The expression of apoptotic proteins and inflammatory pathway-related proteins was detected by Western blotting analysis using the following protein species and antibody sources: Caspase-3(Affinity Biosciences,#AF6311), Bcl-2(Affinity Biosciences,#AF6139), Bax(Affinity Biosciences,#AF0120), Rac-1(Affinity Biosciences,#AF4200), p65(Affinity Biosciences,#AF5006), *p*-p65(Affinity Biosciences,#AF2006). The cell treatment was the same as above, and then the proteins were extracted, gel electrophoresis was performed, the membrane was transferred, the membrane was closed, the primary antibody was incubated for 8 h, and the secondary antibody was incubated for 1 h, and the protein bands were observed by BIO-RAD imaging system, and the intensity of the bands was analyzed by ImageJ software.

Establishment of a rat OA model

With the ethical approval of the Ethics Committee of Guangxi Medical University, the OA model was established using the anterior cruciate ligament transection (ACLT) method in randomized groups of 60 rats, body weight: 200–220 g, male SD rats, and rearing temperature: 23–25 °C. Treatments: weekly injection of drugs and NIR irradiation in the light group twice a week for 5 min each. Samples were collected in batches after 4 and 8 weeks of continuous treatment.

IVIS imaging evaluation

The Cy5-labeled $PtCuO_X/CeO_{2-X}$ and the free Cy5 were injected into a knee joint of the rat. Then the IVIS images were collected by IVIS Spectrum Imaging System (BLT, China) at predetermined times (excitation wavelength 675 nm, emission wavelength 680 nm). In addition, the important organs were also scanned by the IVIS system to clarify the metabolic pathway of $PtCuO_X/CeO_{2-X}$.

Thermographic analysis of rat knee joints

The right knee joints of rats were injected with PBS, CeO_2, and $PtCuO_X/CeO_{2-X}$ (100 μL, 50 μg/mL), respectively. 12 h later, the right knee joints were irradiated with

NIR light. Images and temperatures during NIR irradiation were recorded with an anterior NIR camera.

Gait analysis

After successful modeling of OA, the gait of rats at weeks 4 and 8 was analyzed using the Animal Visual Gait Analysis System. Gait duration and mean gait speed were assessed.

Histologic analysis

Enzyme-linked immunosorbent assay (ELISA)

We used IL-6(MEIMIAN, #MM-0190R2), MMP-13(MEIMIAN, #MM-0110R2), and Col2a1(Zeye Bio, #ZY0324ER) ELISA kits to detect the expression of related proteins in joint fluid and cell supernatants of OA rats, and IL-1β (Solarbio, #SEKR-0002), IL-17 (Solarbio, #SEKR-0007), and TGF-α (Zeye Bio, #ZY0126ER) kits to detect the expression of immune response-related factors. Add specimens according to instructions, incubate at 37 °C for 30 min, and wash 5 times with Wash Solution. Add 50 μL enzyme reagent, incubate for 30 min, wash 5 times, add dyes A and B sequentially, incubate for 10 min at 37 °C without light and add the termination solution. Measure the absorbance (OD value) of each well using an enzyme meter. Calculate the concentration from the standard curve.

Immunohistochemistry staining (IHC)

Tissue sections were routinely deparaffinized and dehydrated using a universal two-step detection kit (ZSGB-BIO, China, #PV-9000), and the antibody was diluted 1:200 and incubated overnight at 4 °C, protected from light, and then conjugated with biotinylated secondary antibody. The slides were photographed with a light microscope (OLYMPUS BX53F, Japan).

Hematoxylin–eosin (HE) and saffron-o-fast green staining

Tissue sections and major organs were stained with hematoxylin–eosin kit (HE, Solarbio, China), saffron-o-fast green staining kit (Solarbio, China), and the sections were observed under a microscope and photographed for histological analysis. In addition, Venous blood samples were collected for routine and blood biochemical analyses to evaluate the biotoxicity of the nanozymes.

Tissue reactive oxygen species assay

Tissue homogenate was prepared by adding 1 mL buffer to 50 mg of knee cartilage tissue, 190 μL supernatant was collected by centrifugation, 10 μL BBcellProbeTM O11 ROS probe (BestBio, China) was added, and the tissue was incubated at 37 °C for 30 min under light protection. The ROS level was determined using a fluorescence microplate reader (Bio-Tek Instruments, USA) with an excitation wavelength of 488 nm and an emission wavelength of 530 nm.

Nanozymes cartilage penetration capability test

100 μL of Cy5-$PtCuO_X/CeO_{2-X}$ (50 μg/mL) was injected into the knee joints of OA rats. The articular cartilage (including subchondral bone) of the femoral and tibial sides of the knee joints were harvested at 24, 48, and 72 h after injection, and the knee joints were immersed in saline for 6 h under light avoidance conditions, and then cryosections were performed, stained with DAPI, and sealed, and the images were visualized and recorded under a fluorescence microscope.

Hemolysis assay

Arterial blood was collected from rats and cell suspension was prepared. Then, 900 μL of ultrapure water (positive control) and PBS containing different concentrations of $PtCuO_X/CeO_{2-X}$ nanozymes were added, and the mixtures were gently shaken and allowed to stand at 37 °C for 2 h. Photographs were taken to compare hemolysis between different groups. The supernatant was transferred to a 96-well plate and the percentage of hemolysis was calculated by recording the absorbance at 540 nm using the enzyme marker.

Statistical analysis

Data were expressed as mean ± standard deviation and found to exhibit a normal/Gaussian distribution under the Shapiro–Wilk test. Analyses were performed using GraphPad Prism software (v. 9.4.1). Unpaired Student's t-test was performed for comparisons between 2 groups, and one-way analysis of variance (ANOVA) was performed for 3 or more groups, followed by Tukey's test. The sample size for each analysis was presented within the figure legends. * and # for $P < 0.05$, ** and ## for $P < 0.01$, *** and ### for $P < 0.001$, and **** and #### for $P < 0.0001$.

Results and discussion

Preparation and characterization of $PtCuO_X/CeO_{2-X}$ nanozymes

CeO_2 nanospheres were synthesized by a hydrothermal method, followed by in situ reduction of Cu and Pt atoms onto CeO_2 nanospheres using hydrazine hydrate to synthesize $PtCuO_X/CeO_{2-X}$ (Fig. 2a). Transmission electron microscopy (TEM) revealed that the particle size of the CeO_2 nanospheres was about 170 nm (Fig. 2b), and their lattice spacing was 0.311 nm (Fig. S1), corresponding to the CeO_2 (111), this crystal surface favors the loading of Cu and Pt nanospheres. As shown in Fig. 2c,d, Cu and Pt nanospheres were uniformly dispersed on the $PtCuO_X$/

CeO_{2-X} nanospheres, and the lattice spacings of 0.224, 0.311, and 0.138 nm corresponded to the PtO_2 (111), CeO_2 (111), and Cu_2O (310), respectively. Notably, after the Cu and Pt nanospheres deposition, the $PtCuO_X/CeO_{2-X}$ nanospheres did not change the size and morphology of CeO_2. Furthermore, the high-angle annular dark-field scanning TEM (HAADF-STEM) image (Fig. 2e) and energy dispersive X-ray spectroscopy (EDS) spectra (Fig. 2f) confirmed the distribution of Ce, O, Cu, and Pt on the $PtCuO_X/CeO_{2-X}$ nanospheres. In addition, Fourier transform infrared spectroscopy (FTIR, Fig. 2g) showed that CeO_2 and $PtCuO_X/CeO_{2-X}$ both exhibited Ce–O bonds at 550 cm^{-1}, indicating that the structure of CeO_2 was not disturbed after Pt and Cu deposition. The X-ray diffraction (XRD, Fig. 2h) pattern of CeO_2 nanospheres shows characteristic peaks at 28.5°, 33.1°, 47.5°, 56.3°, 59.1°, 69.4°, 76.7°, and 79.1° (PDF#43–1002). These peaks correspond to the (111), (200), (220), (311), (222), (400), (331), and (420) crystal planes of CeO_2, respectively, and while $PtCuO_X/CeO_{2-X}$ showed diffraction peaks of CeO_2, the two peaks at 69.8° (PDF # 01–007-0199) and 40.5° (PDP # 37–1087) correspond to Cu_2O (310) and PtO_2 (111), respectively.

The electronic structure of $PtCuO_X/CeO_{2-X}$ was then analyzed by X-ray photoelectron spectroscopy (XPS). The XPS spectrum of $PtCuO_X/CeO_{2-X}$ (Fig. 2i) showed Ce 3d, O 1 s, Cu 2p, and Pt 4f peaks, indicating the successful synthesis of $PtCuO_X/CeO_{2-X}$. The high-resolution Cu 2p spectra of $PtCuO_X/CeO_{2-X}$ showed four fitted peaks at 932.1 eV (Cu^{1+}), 934.6 eV (Cu^{2+}), 952.2 eV (Cu^{1+}), and 955.0 eV (Cu^{2+}), respectively (Fig. 2j and Table S3). The proportion of Cu^{1+} (64.3%, Fig. 2j) in $PtCuO_X/$

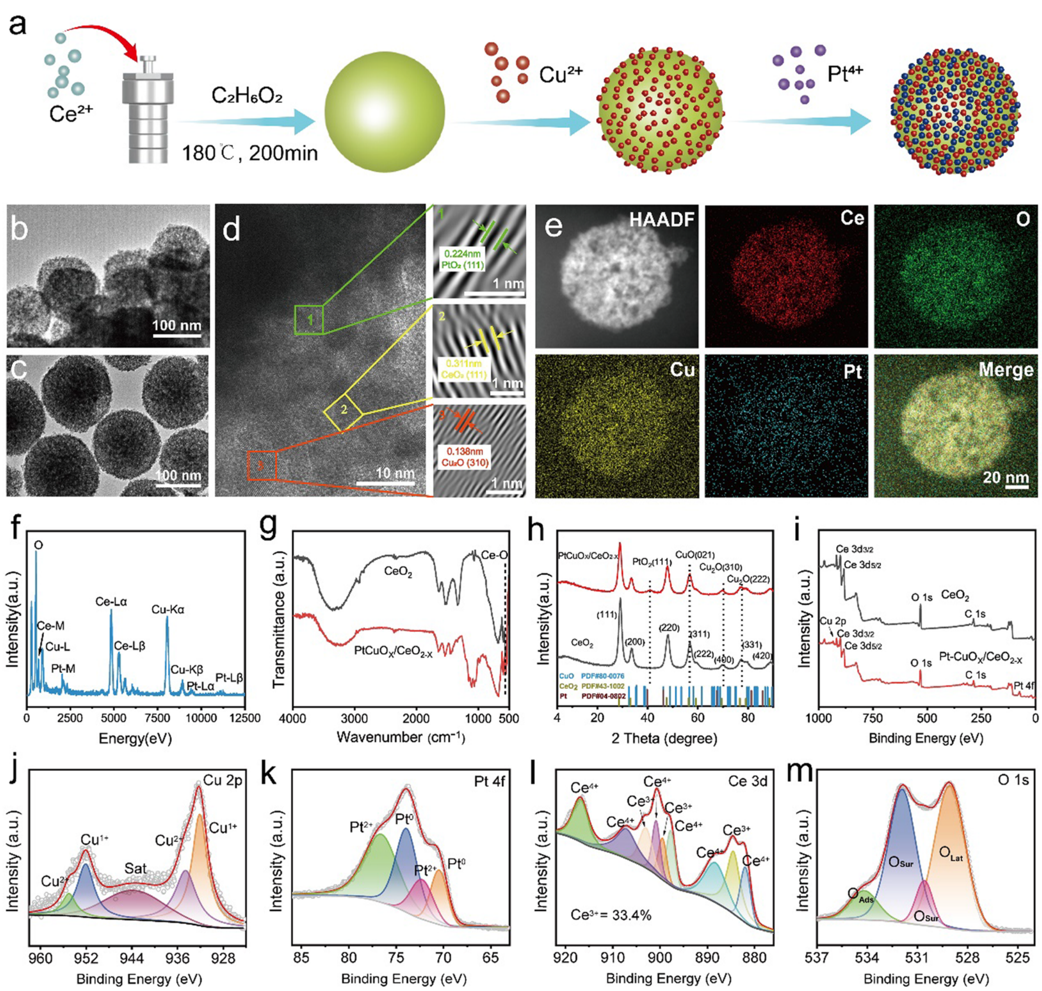

Fig. 2 Synthesis and characterization of $PtCuO_X/CeO_{2-X}$. **a** Schematic diagram of the $PtCuO_X/CeO_{2-X}$ synthesis process. **b** TEM image of CeO_2. **c** TEM image of $PtCuO_X/CeO_{2-X}$. **d** HRTEM image of $PtCuO_X/CeO_{2-X}$, where (I), (II), and (III) represent the lattice spacings of PtO_2, CeO_2, and Cu_2O, respectively. **e** Elemental mapping images and **f** EDS of $PtCuO_X/CeO_{2-X}$. **g** FTIR spectra, **h** XRD pattern of CeO_2 and $PtCuO_X/CeO_{2-X}$. **i** XPS and high-resolution XPS spectra of **j** Cu 2p, **k** Pt 4f, **l** Ce 3d, and **m** O 1 s of $PtCuO_X/CeO_{2-X}$

CeO_{2-X} exceeded that of the intermediate CuO_XCeO_{2-X} (54.3%, Fig. S2a and Table S2). Furthermore, the high-resolution Cu 2p spectra of $PtCuO_X/CeO_{2-X}$ were fitted to obtain Cu^{1+} (932 eV and 952.05 eV), compared with CuO_XCeO_{2-X}, the peak positions of $PtCuO_X/CeO_{2-X}$ were negatively shifted by 0.8 and 0.6 eV, respectively, indicating electron transfer between atoms. In addition, the high-resolution Pt 4f spectra showed four fitted peaks corresponding to 70.5 eV (Pt^0), 72.3 eV (Pt^{4+}), 73.9 eV (Pt^0), and 76.6 eV (Pt^{4+}), respectively (Fig. 2k). At the same time, the high-resolution Ce 3d spectrum of $PtCuO_X/CeO_{2-X}$ showed nine fitted peaks at 882.0 eV (Ce^{4+}), 884.5 eV (Ce^{3+}), 888.3 eV (Ce^{4+}), 897.7 eV (Ce^{4+}), 899.5 eV (Ce^{3+}), 900.8 eV (Ce^{4+}), 903.0 eV (Ce^{3+}), 907.1 eV (Ce^{4+}), and 916.8 eV (Ce^{4+}) (Fig. 2l). Compared to CeO_2 (Fig. S3a and Table S1), the Ce 3d3/2 and Ce 3d5/2 peaks of the $PtCuO_X/CeO_{2-X}$ showed negative shifts of 0.9 eV and 0.5 eV, respectively, suggesting electron transfer between atoms. Importantly, since the Ce^{3+} site of CeO_2 can be considered as an active center mimicking SOD, the higher $Ce^{3+}/(Ce^{3+}+Ce^{4+})$ ratio can promote SOD enzyme-like activity. Furthermore, the higher concentration of Ce^{3+} in CeO_2 also corresponds to a higher oxygen vacancy content [33], [34]. As shown in Fig. 2l, the $Ce^{3+}/(Ce^{3+}+Ce^{4+})$ ratio of $PtCuO_X/CeO_{2-X}$ (33.4%) was higher than that of CeO_2 (26.6%, Fig. S3a). In addition, the split-peak fitting of the CeO_2 spectra resulted in three fitted peaks corresponding to 528.9 eV (O_{Lat}: O_2^-), 530.7 eV (O_{Sur}: O_2^{2-}, O_2^-), and 532 eV (O_{Ads}: -OH, CO_3^{2-}) (Fig. S3b). The high-resolution O 1 s spectra of $PtCuO_X/CeO_{2-X}$ show four peaks corresponding to 529.0 eV (O_{Lat}: O_2^-), 530.5 eV, and 531.9 eV (O_{Sur}: O_2^{2-}, O_2^-), and 534.2 eV (O_{Ads}: -OH, CO_3^{2-}), respectively. Compared with the CeO_2 (1.08), $PtCuO_X/CeO_{2-X}$ (1.24) had a higher O_{Sur}/O_{Lat} ratio, which may be due to the presence of more oxygen vacancies after Cu and Pt doping (Fig. 2m) [35]. And the higher concentration of surface oxygen vacancies is beneficial for the adsorption and activation of ROS and RNS, as well as for the enhancement of SOD/CAT-like activity [36]. Therefore, the XPS results not only further confirmed the successful synthesis of $PtCuO_X/CeO_{2-X}$, but also proved its high oxygen vacancy exposure and strong inter-elemental electron transfer interactions, which were beneficial for improving the catalytic performance of $PtCuO_X/CeO_{2-X}$ nanozymes.

In addition, $PtCuO_X/CeO_{2-X}$ can be uniformly dispersed in PBS, 5% H_2O_2, fetal bovine serum, and culture medium containing 10% fetal bovine serum within 7 days (Fig. S4). The results showed that the hydration particle size and PDI of $PtCuO_X/CeO_{2-X}$ remained similar within 7 days, indicating their good dispersion stability in physiological environments.

Photothermal conversion performance and enzyme-like activity of $PtCuO_X/CeO_{2-X}$ nanozymes

As shown in Fig. 3a,b, after 15 min of irradiation with NIR light (808 nm), the PBS buffer and CeO_2 maintained 27.6 °C and 30.9 °C, respectively. However, the $PtCuO_X/CeO_{2-X}$ increased to 48.5 °C, indicating that the deposition of Cu and Pt on CeO_2 greatly improves its photothermal conversion performance. The photothermal conversion efficiency of the $PtCuO_X/CeO_{2-X}$ was measured to be 55.41% (Fig. S5c,d), which was higher than that of the CeO_2 (26.88%, Fig. S5a,b). The photothermal performance of $PtCuO_X/CeO_{2-X}$ increased with higher $PtCuO_X/CeO_{2-X}$ concentration (Fig. S6a) and higher irradiation power (Fig. S6b). In addition, the $PtCuO_X/CeO_{2-X}$ nanospheres showed no temperature decrease during four repeated "heating/cooling" cycles (Fig. 3c), indicating their good photothermal stability.

SOD-catalyzed scavenging of $\cdot O_2^-$ is the first line of defense for the body's antioxidant response [37]. As shown in Fig. 3d, in the electron spin resonance (ESR) map, compared with the blank and CeO_2, $PtCuO_X/CeO_{2-X}$ reduced the characteristic signals of $\cdot O_2^-$. Under NIR light irradiation, the characteristic signal was further decreased. The SOD enzyme activity test result (Fig. 3e) was consistent with the above conclusion, CeO_2, $PtCuO_X/CeO_{2-X}$, and $PtCuO_X/CeO_{2-X}$ + NIR had $\cdot O_2^-$ scavenging ratios of 22.75%, 47.89%, and 58.84%, respectively, indicating that they had superior $\cdot O_2^-$ scavenging ability and SOD-like enzyme activity. In addition, the SOD reaction subsequently generated H_2O_2, which was then decomposed by $PtCuO_X/CeO_{2-X}$, mimicking the CAT enzyme activity, to produce O_2 and H_2O. As shown in Fig. 3f,g and Fig. S7. $PtCuO_X/CeO_{2-X}$ exhibited superior CAT-like enzyme activity by decomposing a larger amount of oxygen produced from the H_2O_2 reaction compared to PBS and CeO_2, NIR light irradiation effectively enhanced the catalytic activity of the enzyme. In addition, the SOD/CAT enzyme-like activities of the $PtCuO_X/CeO_{2-X}$ showed concentration dependence as shown in Fig. S8. Furthermore, by repeatedly adding the same amount of H_2O_2 to the $PtCuO_X/CeO_{2-X}$ solution, it was found that the rate and level of O_2 production remained constant each time, indicating that $PtCuO_X/CeO_{2-X}$ exhibited stable and sustained CAT-like activity (Fig. 3h). Similarly, $PtCuO_X/CeO_{2-X}$ also exhibited superior ·OH scavenging ability compared to CeO_2, and the scavenging activity was further enhanced under NIR light irradiation. Compared to CeO_2 (25.82%) and $PtCuO_X/CeO_{2-X}$ (40.09%), $PtCuO_X/CeO_{2-X}$ + NIR showed excellent scavenging of ·OH (51.13%, Fig. 3i, j). When tested with ABTS probes, $PtCuO_X/CeO_{2-X}$ showed a superior ability to scavenge total ROS, which is consistent with the above results

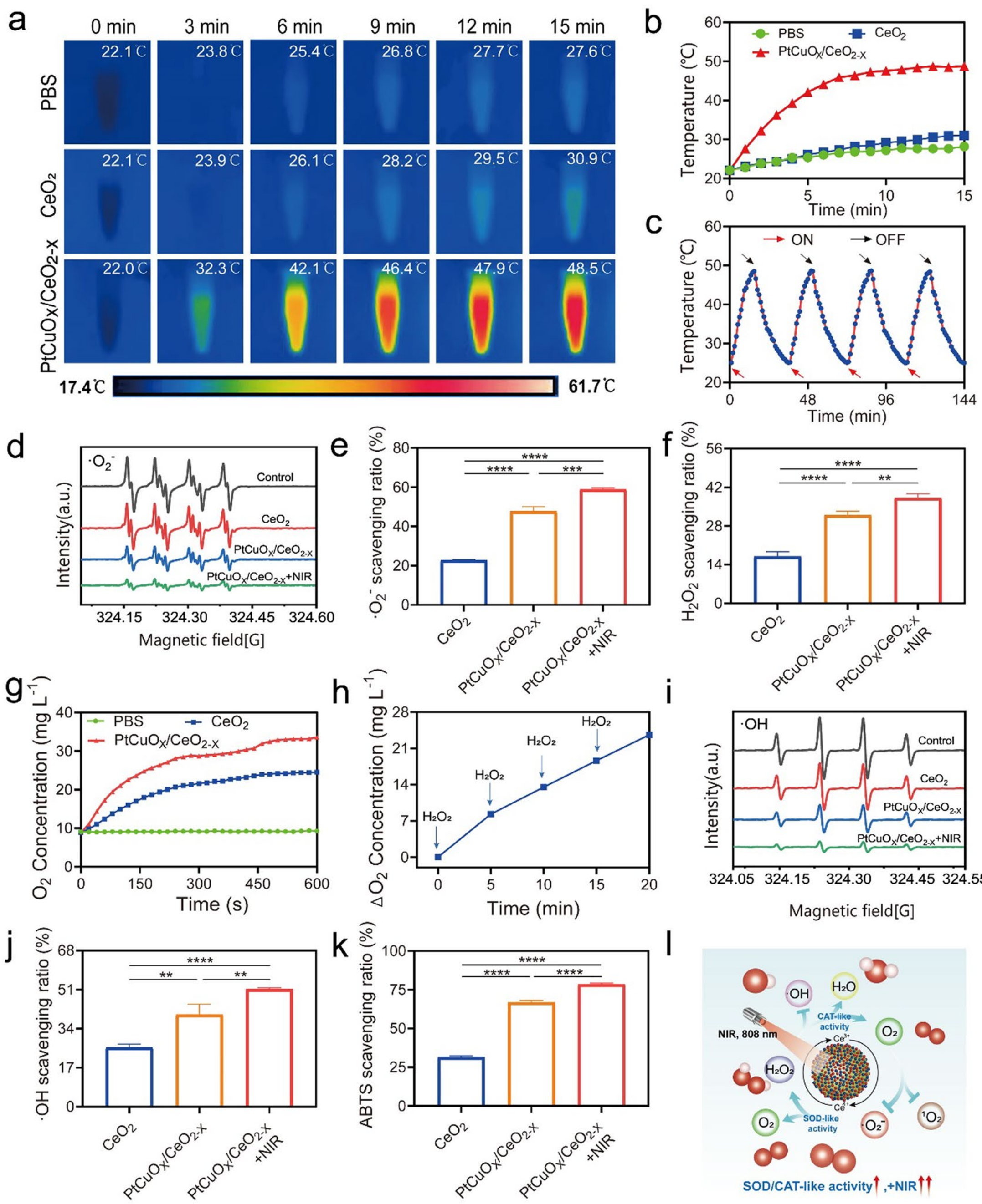

Fig. 3 Photothermal characterization and free radical scavenging ability of $PtCuO_X/CeO_{2-X}$ nanozymes. **a** Photothermal images and **b** photothermal curves of PBS, CeO_2, and $PtCuO_X/CeO_{2-X}$ (50 µg/mL, 808 nm, 1.0 W/cm^2). **c** Photothermal curve of $PtCuO_X/CeO_{2-X}$ (50 µg/mL, 808 nm, 1.0 W/cm^2) to analyze the heating and cooling temperature profiles. **d** The $\cdot O_2^-$ scavenging ability measured by ESR. **e** SOD and **f** CAT activity measured by ROS detection kit. **g** Oxygen content from decomposition of H_2O_2 by PBS, CeO_2, and $PtCuO_X/CeO_{2-X}$. **h** Oxygen content in the aqueous solution of $PtCuO_X/CeO_{2-X}$ was measured after repeated addition of H_2O_2. **i** ·OH scavenging ability measured by ESR. **j** Scavenging ability of CeO_2, $PtCuO_X/CeO_{2-X}$, and $PtCuO_X/CeO_{2-X}$ + NIR was evaluated for ·OH. **k** for ABTS. **l** Schematic diagram of the antioxidant process of $PtCuO_X/CeO_{2-X}$ nanozymes. Data are expressed as mean ± SD (n = 3). * and # for $P < 0.05$, ** and ## for $P < 0.01$, *** and ### for $P < 0.001$, and **** and #### for $P < 0.0001$

(Fig. 3k). RNS scavenging also contributed to the protection of chondrocytes from oxidative stress damage and the restoration of mitochondrial function. Fortunately, $PtCuO_X/CeO_{2-X}$ also showed good RNS scavenging ability. The DPPH scavenging rates of $PtCuO_X/CeO_{2-X}$ and $PtCuO_X/CeO_{2-X}$ + NIR were 24.91% and 34.35%, respectively, surpassing that of CeO_2 (15.67%, Fig. S9). Therefore, $PtCuO_X/CeO_{2-X}$ nanozymes have photo-enhanced SOD/CAT enzyme activity as well as an excellent ability to scavenge ROS/RNS (Fig. 3l), which is expected to alleviate oxidative stress in the treatment of OA.

DFT studies on the enzyme activity of $PtCuO_X/CeO_{2-X}$ nanozymes

We used density functional theory (DFT) calculations to investigate the origin of the high SOD/CAT-like catalytic efficiency of $PtCuO_X/CeO_{2-X}$ nanozymes. Based on the characterization results, we constructed a simulated model of $PtCuO_X/CeO_{2-X}$ (Fig. S10). The partial density of states (PDOS) of $PtCuO_X/CeO_{2-X}$ nanozymes showed a significant overlap between the Cu, Pt, and CeO_2, indicating a strong orbital hybridization and interaction among them (Fig. 4a). The differential charge map of $PtCuO_X/CeO_{2-X}$ nanozymes showed the electron transfer between Cu, Pt, and Ce, which facilitated the stabilization of Pt and Cu dispersion on CeO_2 (Fig. 4b). Importantly, the oxygen vacancy formation energy of $PtCuO_X/CeO_{2-X}$ nanozymes (2.39 eV) was found to be lower than that of CeO_2 (2.55 eV, Fig. 4c,d), indicating that the introduction of Cu and Pt on the CeO_2 contributed to the formation of oxygen vacancies, which was consistent with the above conclusion. In addition, the $PtCuO_X/CeO_{2-X}$ nanozymes exhibited higher adsorption energies for H_2O_2, O_2, O, and H_2O compared to CeO_2 (Fig. S11a and Table S4). Compared to the CeO_2, the differential charge distribution map of $PtCuO_X/CeO_{2-X}$ nanozymes showed electron transfer between the $PtCuO_X/CeO_{2-X}$ nanozymes, further stabilizing the small molecules on the surface (Fig. 4e and Fig. S11b). There was a stronger overlap between Cu d-orbitals, Pt d-orbitals, and O 2p orbitals with P orbitals of small molecules, indicating enhanced adsorption of reaction intermediates by $PtCuO_X/CeO_{2-X}$, which was beneficial for $PtCuO_X/CeO_{2-X}$ nanozymes to catalyze SOD/CAT reactions of small molecules.

For the SOD-like catalyzed reaction (Fig. 4f), the reaction adsorption energies of $PtCuO_X/CeO_{2-X}$ nanozymes were lower than those of CeO_2 at each step (Fig. 4g), indicating that $PtCuO_X/CeO_{2-X}$ nanozymes convert $\cdot O_2^-$ to H_2O_2 and O_2 more readily than CeO_2. Notably, the rate-limiting step of the SOD-catalyzed process was identified as $\cdot O_2^- + 2H^+ + Cluster^+ \rightarrow H_2O_2 + Cluster^{2+}$. The energy barrier for this rate-determining step was reduced by $PtCuO_X/CeO_{2-X}$ nanozymes (0.22 eV) compared to CeO_2 (0.76 eV), suggesting that the kinetics of the SOD reaction on $PtCuO_X/CeO_{2-X}$ were significantly enhanced. We used the same analytical method to map the energy distribution of H_2O_2 decomposition on CeO_2 and $PtCuO_X/CeO_{2-X}$ nanozymes (Fig. 4h, i). The CAT reaction starts as $H_2O_2 \rightarrow {}^*H_2O_2 \rightarrow {}^*H_2O + {}^*O$. The adsorption energy of H_2O_2 on $PtCuO_X/CeO_{2-X}$ (-0.6 eV) is higher than its adsorption on CeO_2 (-0.07 eV, Fig. S11a), indicating that H_2O_2 is more easily adsorbed on $PtCuO_X/CeO_{2-X}$ than on CeO_2, which is more favorable for the subsequent cleavage reaction. In addition, the dissociation of adsorbed H_2O_2 into OH ($H_2O_2 \rightarrow 2OH$) is the rate-limiting step for $PtCuO_X/CeO_{2-X}$ nanozymes to exert CAT enzyme-like effects. Compared with CeO_2 (0.83 eV), $PtCuO_X/CeO_{2-X}$ nanozymes (0.54 eV) exhibited a lower energy barrier for the rate-determining step, which significantly enhanced the CAT reaction kinetics. Therefore, compared with CeO_2, $PtCuO_X/CeO_{2-X}$ nanozymes can increase the oxygen vacancies and have stronger electron transfer interaction, thus facilitating the adsorption energy for reaction intermediates and lowering the energy barrier, which improved the SOD/CAT-like reaction kinetics and enzyme catalytic activity.

In vitro study of $PtCuO_X/CeO_{2-X}$ nanozymes for ROS/RNS scavenging and mitochondrial function protection

Excessive ROS and RNS promote the expression of inflammatory factors and also induce chondrocyte apoptosis and extracellular matrix degradation, accelerating the development of OA [38]. To investigate this, IL-1β-induced chondrocytes were used as an in vitro model [39]. The optimal concentration for cell growth was first determined using a CCK-8 assay (Fig. S12a). Based on the results, it was observed that the cell activity remained more than 90% in the range of 80 μg/mL, and the best cell activity was observed at the concentration of 50 μg/mL, which was therefore selected as the concentration for subsequent validation. Subsequently, as shown in Fig. S12b, cell viability was severely inhibited in the IL-1β-induced inflammation group, while CeO_2 and $PtCuO_X/CeO_{2-X}$ nanozymes were able to rescue damaged chondrocytes, and this effect was further enhanced by NIR light irradiation. Consistent with the results of live-dead staining in Fig. S13a, there were a large number of dead chondrocytes (red signals) in the inflammation group, the live/dead ratio of chondrocytes after IL-1β stimulation was 3.71%, CeO_2, $PtCuO_X/CeO_{2-X,}$ and $PtCuO_X/CeO_{2-X}$ + NIR treatments were increased to 8.02%, 12.08%, and 19.92%, respectively (Fig. S13b). The results in Fig. S14 showed the presence of Cy5-labeled $PtCuO_X/CeO_{2-X}$ red fluorescence signal in chondrocytes, which gradually increased within 12 h, indicating that the $PtCuO_X/CeO_{2-X}$ nanozymes were effectively taken up by the cells.

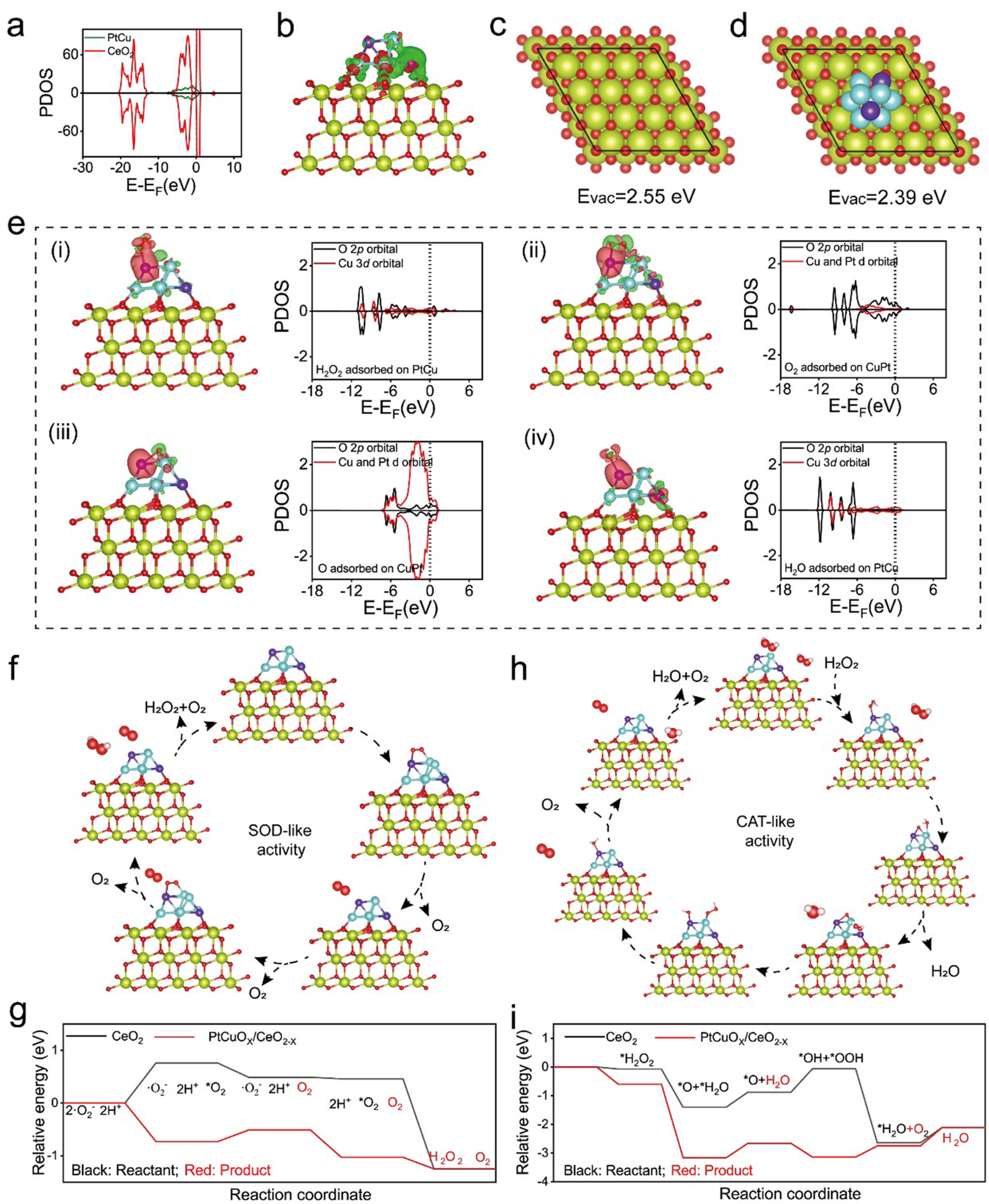

Fig. 4 DFT study on the SOD and CAT activities of $PtCuO_X/CeO_{2-X}$ nanozymes. **a** PDOS and **b** differential charge density map of $PtCuO_X/CeO_{2-X}$. **c** Calculation of the oxygen vacancy formation energy of CeO_2 and **d** $PtCuO_X/CeO_{2-X}$. **e** Differential charge density map and PDOS of different adsorbates (H_2O_2, O_2, O, H_2O) adsorbed on the surface of $PtCuO_X/CeO_{2-X}$. **f** Proposed catalytic mechanism and **g** Free energy diagrams for SOD-like activity of CeO_2 and $PtCuO_X/CeO_{2-X}$. h) Proposed catalytic mechanism and **i** Free energy diagrams for CAT-like activity of CeO_2 and $PtCuO_X/CeO_{2-X}$

Detection of intracellular ROS and RNS scavenging capacity was performed using specific fluorescent probes, including ROS, $\cdot O_2^-$, ·OH, NO, and O_2 (Fig. 5a,b and Fig. S15). Minimal fluorescence signals were observed in the control group. However, upon IL-1β induction, the fluorescence signals were significantly enhanced, indicating the generation of a substantial amount of ROS and RNS. Compared with a slight decrease in fluorescence intensity of the CeO_2 group, the $PtCuO_X/CeO_{2-X}$ group showed a significant decrease in fluorescence intensity, which was better under the NIR irradiation.

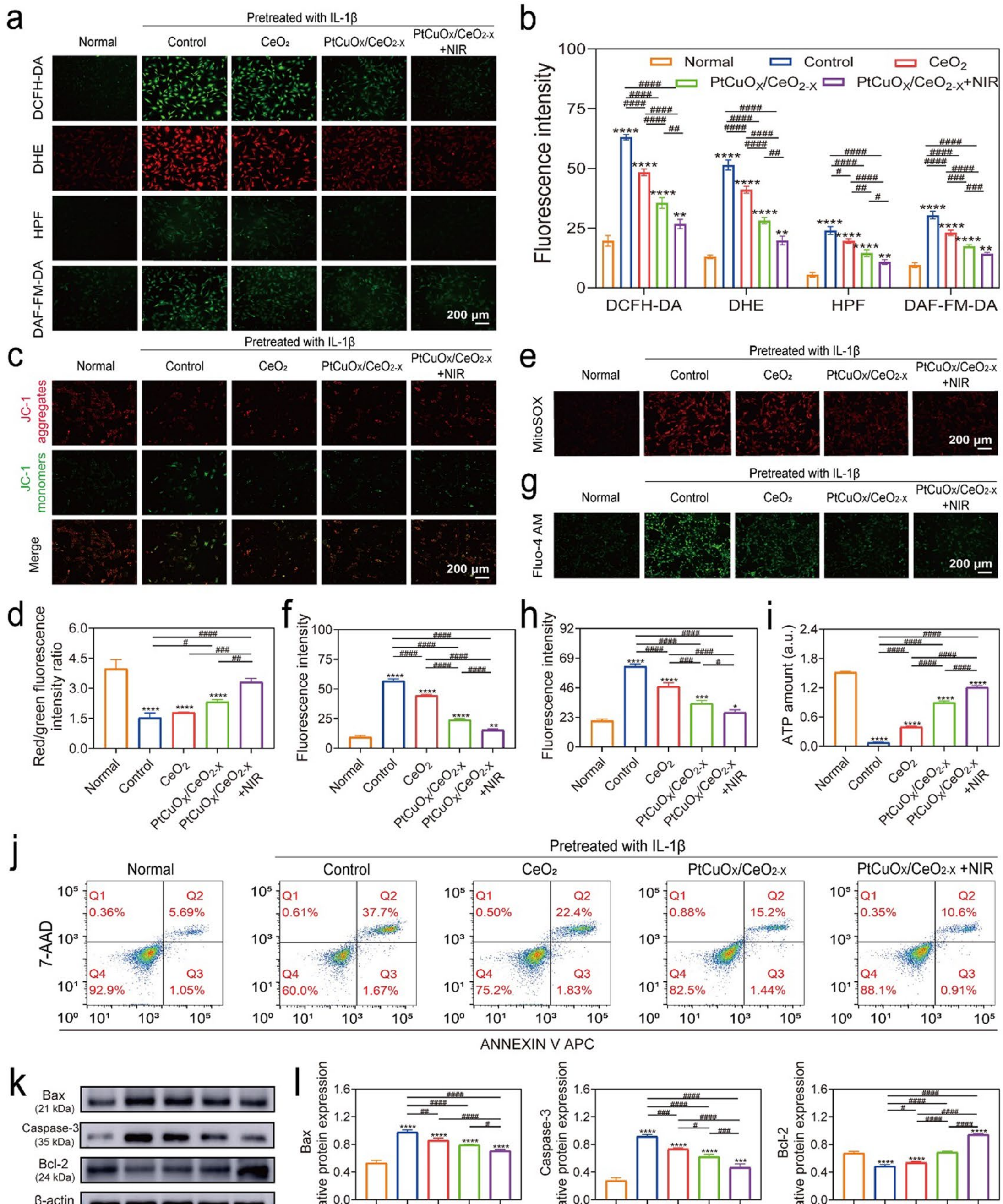

Fig. 5 ROS scavenging, mitochondrial protection, and apoptosis inhibition by $PtCuO_X/CeO_{2-X}$ nanozymes in vitro. **a** Chondrocyte staining with various ROS assay kits and **b** corresponding quantification to assess the scavenging capacity of ROS, $\cdot O_2^-$, ·OH, and NO, respectively. **c** Chondrocyte staining with mitochondrial membrane potential probe (JC-1) and **d** corresponding quantification to assess the membrane potential. **e** Chondrocyte staining with MitoSOX probe and **f** corresponding quantification to assess the level of endogenous ROS. **g** Chondrocyte staining with Fluo-4 AM probe and **h** corresponding quantification to assess the disturbance of Ca^{2+} efflux. **i**) ATP assay kit to assess ATP levels in chondrocytes after different treatments. **j** 7-AAD/Annexin V-APC apoptosis kit to assess apoptosis in chondrocytes after different treatments. **k** Western blotting and **l** quantitative analysis to assess Bax, Caspase-3, and Bcl-2 protein levels. Concentration: 50 μg/mL; NIR parameters: 808 nm, 1.0 W/cm^2, 5 min. Data are expressed as mean ± SD (n = 3). * and # for P < 0.05, ** and ## for P < 0.01, *** and ### for P < 0.001, and **** and #### for P < 0.0001

The ROS/RNS are products of mitochondrial energy metabolism, scavenging excessive ROS/RNS can restore mitochondrial dysfunction, thus delaying OA. As shown in Fig. 5c,d, IL-1β-induced chondrocytes exhibited increased green fluorescence (JC-1 monomers) and decreased red fluorescence (JC-1 aggregates), suggesting that mitochondrial damage led to a decrease in membrane potential. With the treatment of CeO_2, $PtCuO_X/CeO_{2-X}$, $PtCuO_X/CeO_{2-X}$ + NIR, the red fluorescence gradually increased and the green fluorescence gradually decreased, indicating that $PtCuO_X/CeO_{2-X}$ can significantly ameliorate the mitochondrial damage, even better under NIR irradiation. The results of the JC-1 flow cytometry were consistent with the above results (Fig. S16). Similarly, the $PtCuO_X/CeO_{2-X}$ + NIR group was more effective in scavenging mitochondrial ROS compared to the other four groups (Fig. 5e, f). In addition, IL-1β induced an increase in intracellular Ca^{2+} accumulation compared to the normal group, indicating impaired intracellular Ca^{2+} homeostasis due to mitochondrial damage. However, the abnormal Ca^{2+} accumulation was reduced by the CeO_2, $PtCuO_X/CeO_{2-X}$, especially $PtCuO_X/CeO_{2-X}$ + NIR, indicating the strong mitochondrial protective effect (Fig. 5g,h). Furthermore, the adenosine triphosphate (ATP) content was used to evaluate the intracellular energy metabolism [40]. As shown in Fig. 5i, and Fig. S17, $PtCuO_X/CeO_{2-X}$ + NIR significantly promoted ATP production in IL-1β-induced cells, which was more significant than CeO_2 and $PtCuO_X/CeO_{2-X}$.

$PtCuO_X/CeO_{2-X}$ nanozymes have excellent SOD/CAT enzyme activity, and their catalytic activity can be enhanced by photo thermolysis, which can effectively remove ROS/RNS, restore mitochondrial function and protect chondrocytes from apoptosis. As shown in Fig. 5j, the apoptosis rate of chondrocytes was gradually decreased by the CeO_2 (22.4%), $PtCuO_X/CeO_{2-X}$ (15.2%), and $PtCuO_X/CeO_{2-X}$ + NIR (10.6%) groups compared with the IL-1β group (37.7%). Mechanistically, Bax, Caspase-3, and Bcl-2 [41–43], as key apoptotic factors in their activated state, can provide insights into the intrinsic properties of $PtCuO_X/CeO_{2-X}$ nanozymes in inhibiting apoptosis. Fig. S18 shows an increase in the expression of Bax and Caspase-3 and a decrease in Bcl-2 in the IL-1β group. However, compared with the control and CeO_2 groups, $PtCuO_X/CeO_{2-X}$ nanozymes effectively reversed these changes, and the effect was further enhanced by NIR irradiation. The above results were further confirmed by Western blot analysis (Fig. 5k, l).

$PtCuO_X/CeO_{2-X}$ nanozymes reduce oxidative stress for anti-inflammatory effects

Inflammatory degeneration was a typical feature of OA progression [44]. To elucidate the anti-inflammatory capacity of $PtCuO_X/CeO_{2-X}$ nanozymes, we performed gene expression analysis of relevant inflammatory markers. It is well known that interleukin 6 (IL-6), in addition to matrix metalloproteinase 13 (MMP-13), plays a key role in the induction of matrix-degrading enzymes that contribute to cartilage degeneration and metastasis. In contrast, Col2a1 is a critical component of the extracellular matrix essential for cartilage regeneration [45–47]. Figure 6a showed that the IL-1β group had higher fluorescence intensity (IL-6 and MMP-13) and lower expression of Col2a1 compared to the normal group. However, the expression of IL-6 and MMP-13 induced by IL-1β was reversed by CeO_2 and $PtCuO_X/CeO_{2-X}$ treatments. Moreover, under NIR irradiation, the effect of $PtCuO_X/CeO_{2-X}$ was even more significant (Fig. 6b).

In addition, the results of quantitative real-time polymerase chain reaction (qRT-PCR) showed that compared with the normal group, MMP-13, IL-6, tumor necrosis factor α (TNF-α), and inducible nitric oxide synthase (iNOS) were significantly upregulated, while Col2α1 and aggregated proteoglycan (ACAN) were significantly downregulated in the IL-1β group [48–50]. Compared with the IL-1β group, CeO_2, and $PtCuO_X/CeO_{2-X}$ nanozymes decreased the expression of inflammatory genes, especially under NIR irradiation. And $PtCuO_X/CeO_{2-X}$ + NIR group also increased the expression of ACAN and Col2a1 (Fig. 6c). The results of the ELISA test further confirmed the above results (Fig. S19).

Mechanistically, the ROS/Rac-1/NF-κB pathway plays a key role in accelerating the progression of OA during the inflammatory response, catabolism, and apoptosis [51]. In OA, overproduction of ROS is involved in multiple signaling pathways activated by injury or cytokines, including causing an increase in the activation of ras-related C3 botulinum toxin substrate 1 (Rac-1) and activation of the nuclear factor-κB (NF-κB) pathway to amplify the inflammatory response [52, 53]. Aberrant activation of Rac-1 and NF-κB can exacerbate joint damage by promoting tissue inflammation, synthesis of catabolic factors, and apoptosis of articular chondrocytes [54. Further, in the activated state, the IκB protein in the cytoplasm is phosphorylated and degraded upon chemical or mechanical stimulation. Subsequently, NF-κB dimers are released and translocated to the nucleus to induce transcription of target genes. In response to IL-1β, NF-κB is markedly upregulated, promotes nuclear translocation of p65, activates Rac-1, and contributes to the progression of inflammation [55]. Western blotting analyses showed that the $PtCuO_X/CeO_{2-X}$ nanozymes significantly inhibited IL-1β-induced elevation of Rac-1 protein levels and *p*-p65/p65 ratio, and this effect was enhanced under NIR irradiation (Fig. 6d-f). Therefore, $PtCuO_X/CeO_{2-X}$ nanozymes remodel the IL-1β-induced

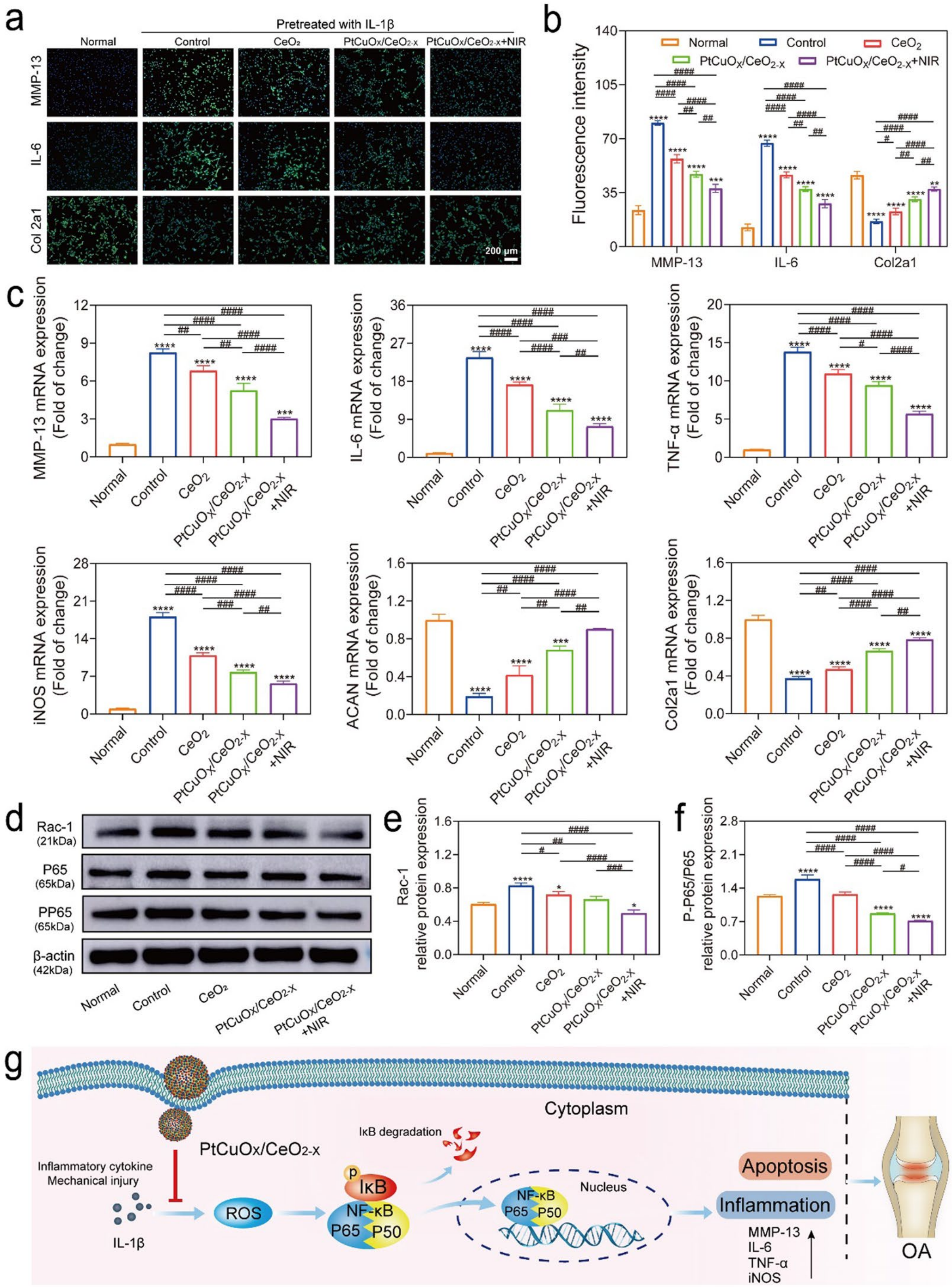

Fig. 6 Anti-inflammatory and protective effects of $PtCuO_X/CeO_{2-X}$ nanozymes at the cellular level and their mechanisms. **a** Fluorescence images and **b** quantification of fluorescence intensity of immunofluorescence staining (MMP-13, IL-6, and Col2a1) of chondrocytes to evaluate relative protein expression levels. **c**) Relative RNA expression levels of inflammatory genes (MMP-13, IL-6, TNF-α, iNOS,) and chondrocyte-specific genes (ACAN and Col2a1) in chondrocytes after different treatments evaluated by qRT-PCR. **d** Western blot and **e**–**f** quantification analysis to evaluate the protein levels of Rac1, *p*-p65, and p65. **g** Mechanism of action of $PtCuO_X/CeO_{2-X}$ nanozymes on ROS/Rac-1/NF-κB signaling pathway. Concentration: 50 μg/mL; NIR Parameters: Wavelength: 808 nm, Power: 1.0 W/cm^2, and Duration: 5 min. Data are expressed as mean ± SD (n = 3). * and # for P < 0.05, ** and ## for P < 0.01, *** and ### for P < 0.001, and **** and #### for P < 0.0001

microenvironment in chondrocytes by attenuating the ROS/Rac-1/NF-κB signaling pathway, thereby ameliorating OA (Fig. 6g).

In vivo study of $PtCuO_X/CeO_{2-X}$ nanozymes for OA therapy

To further evaluate the therapeutic effect of $PtCuO_X/CeO_{2-X}$ nanozymes on OA in vivo, we established an OA model using anterior cruciate ligament dissection (ACLT) [56] (Fig. 7a). The in vivo photothermal effect of $PtCuO_X/CeO_{2-X}$ nanozymes confirmed their potential for photothermal therapy (Fig. 7b,c). $PtCuO_X/CeO_{2-X}$ nanoparticles had cartilage penetration ability and could effectively penetrate the extracellular matrix into the cartilage layer and even the subchondral bone (Fig. S20). In addition, $PtCuO_X/CeO_{2-X}$ was mainly metabolized through the hepatic and renal pathways after intra-articular injection and was cleared within 1 week (Fig. S21). Interestingly, $PtCuO_X/CeO_{2-X}$ did not induce immune rejection. (Fig. S22 and Fig. S23). As shown in Fig. 7d, after 4 and 8 weeks of treatment, the femoral and tibial articular surfaces and cartilage surfaces were smooth in the sham group. However, in the OA group, the articular cartilage layer showed obvious wear, with concave and convex surfaces, as well as obvious bone erosion and fissures, indicating the successful establishment of the OA rat model. After treatment with $PtCuO_X/CeO_{2-X}$ nanozymes, cartilage damage, and erosion were significantly reduced, and the effect was better under NIR irradiation. Based on the Pelletier score [57], the $PtCuO_X/CeO_{2-X}$ + NIR group showed a significant decrease in score compared to the OA group, with a decrease of 60.51% and 60.91% at 4 and 8 weeks, respectively (Fig. 7e). Next, hematoxylin and eosin (H&E) staining (Fig. 7f) and safranin O staining (Fig. 7g) showed significant fissures, matrix loss, thin and irregular cartilage layer, and significant cartilage layer destruction in the OA group compared with the normal group. Fortunately, $PtCuO_X/CeO_{2-X}$ nanozymes can effectively reverse the above pathological changes, especially after supplementation with NIR radiation, and the articular surface can be restored to a near-normal level. Finally, according to the OARSI score [58] (Fig. 7h), after treatment with $PtCuO_X/CeO_{2-X}$ nanozymes, the score decreased by 46.65% compared with the OA group and significantly decreased by 74.15% under NIR irradiation. Therefore, $PtCuO_X/CeO_{2-X}$ nanozymes exhibit significant cartilage protection with the assistance of NIR irradiation.

Immunohistochemical staining showed that the OA group had the highest number of brown heterostained particles, indicating a significant expression of MMP-13, IL-6, Rac-1, and *p*-p65. However, the $PtCuO_X/CeO_{2-X}$ nanozymes downregulated the expression of the above proteins beyond the effect of CeO_2 alone. Moreover, the effect was further enhanced under NIR irradiation. In addition, compared with CeO_2 alone, $PtCuO_X/CeO_{2-X}$ nanozymes upregulated the expression level of Col2a1 protein, indicating that it promoted cartilage repair (Fig. 8a and Fig. S24). Next, an ELISA assay to assess the level of expression of inflammatory factors in the synovial fluid yielded results consistent with those described above (Fig. 8b). Meanwhile, the ROS content in articular cartilage of the OA group was 14.52 times higher than that of the sham group. The ROS content of CeO_2, $PtCuO_X/CeO_{2-X,}$ and $PtCuO_X/CeO_{2-X}$ + NIR group in articular cartilage gradually decreased. Especially, the $PtCuO_X/CeO_{2-X}$ + NIR group showed a 68% decrease, indicating that it had the best effect in scavenging ROS from articular cartilage (Fig. S25). Under the ROS persisted, $PtCuO_X/CeO_{2-X}$ continued to exert antioxidant effects [59] (Fig. S26). Next, as shown in Fig. 8c-e, the results of gait analysis indicated that the $PtCuO_X/CeO_{2-X}$ + NIR group showed the most favorable recovery in walking time and average walking speed compared to the OA group.

Finally, the result of H&E staining (Fig. S27) indicated that the major organs showed no significant histopathological necrosis or inflammatory lesions, suggesting that there was no internal organ damage during the OA treatment with $PtCuO_X/CeO_{2-X}$ nanozymes. Similarly, the results of the hemolysis experiment further supported the above findings (Fig. S28). The results of blood biochemical analysis in rats showed no difference in biochemical indicators in the $PtCuO_X/CeO_{2-X}$ + NIR group compared with the sham group (Fig. S29). Therefore, $PtCuO_X/CeO_{2-X}$ nanozymes have good biosafety in vivo and have excellent potential for the treatment of OA.

Conclusion

In summary, according to the "defect engineering construction strategy", we developed $PtCuO_X/CeO_{2-X}$ nanozymes as highly efficient SOD/CAT mimics by introducing bimetallic Cu and Pt into CeO_2 nanospheres to enhance the oxygen vacancies, in an attempt to combine NIR irradiation to regulate microenvironment for OA therapy. Doping Cu and Pt on CeO_2 significantly increased the Ce^{3+}/Ce^{4+} ratio to enhance the oxygen vacancies, while CeO_2(111) promoted the homogeneous dispersion of Cu and Pt. In particular, the DFT results proved that the $PtCuO_X/CeO_{2-X}$ nanozymes decreased the oxygen vacancy formation energy, promoted electron transfer, exposed the active center, increased the interfacial adsorption energy, and decreased the reaction activation energy, thus improving the SOD/CAT-like activity. Besides, the nanozymes have excellent photothermal conversion efficiency (55.41%). Further, $PtCuO_X/CeO_{2-X}$

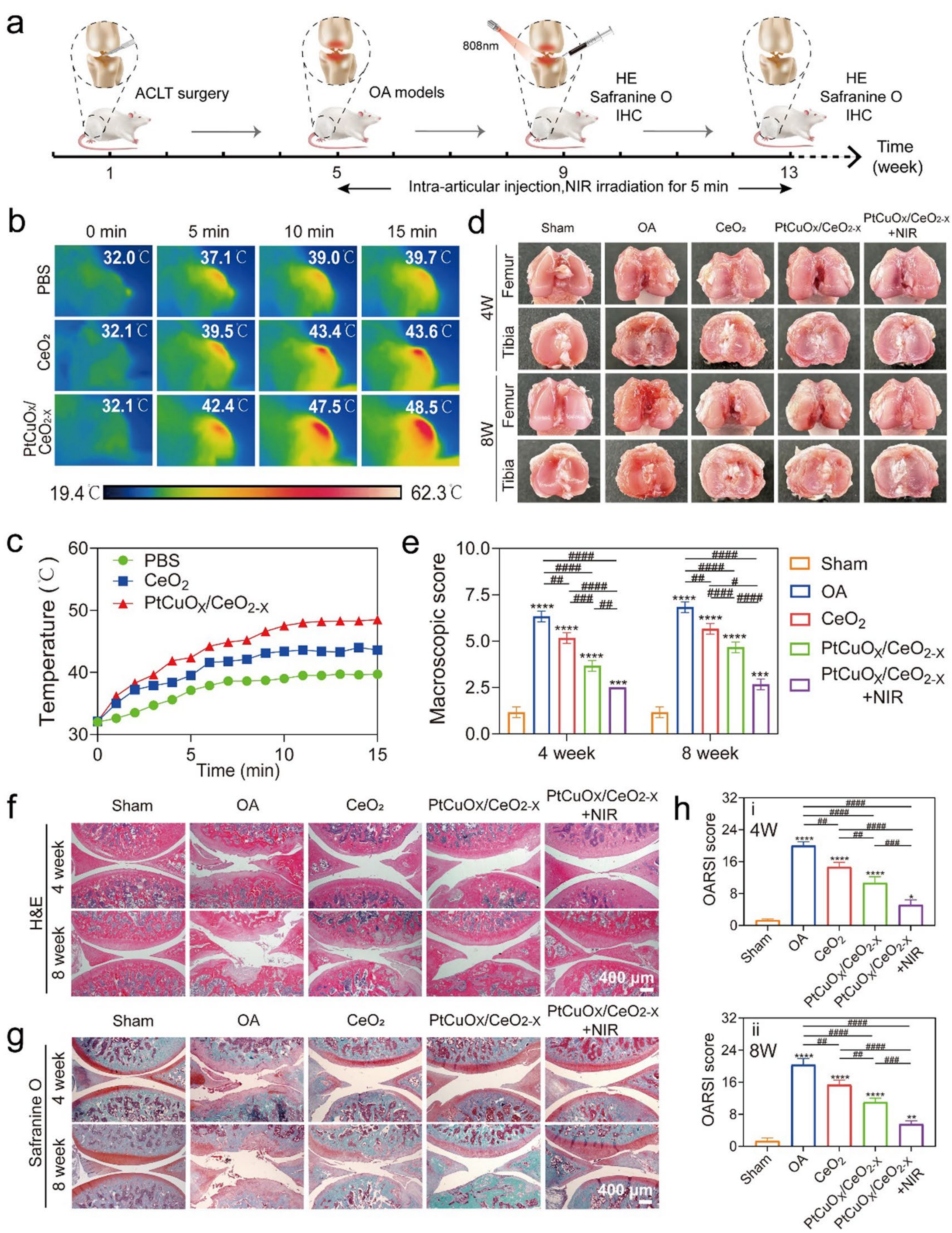

Fig. 7 PtCuO$_X$/CeO$_{2-X}$ nanozymes alleviate the ACLT model in rats. **a** Schematic illustration of the PtCuO$_X$/CeO$_{2-X}$ therapeutic process. **b** Photothermal images and **c** photothermal curves of rat knee joints after the injection of PBS, CeO$_2$, and PtCuO$_X$/CeO$_{2-X}$, respectively. **d** Gross observations and **e** macroscopic scores of knee joints at 4 and 8 weeks. **f** HE stained images, **g** safranin O staining, and **h** OARSI scores of knee joints at 4 and 8 weeks. Concentration: 50 μg/mL and 100 μL per injection, with injections once a week. NIR Parameters: Wavelength: 808 nm, Power: 1.0 W/cm^2, and Duration: 5 min. Data are expressed as mean ± SD (n = 3). * and # for P < 0.05, ** and ## for P < 0.01, *** and ### for P < 0.001, and **** and #### for P < 0.0001

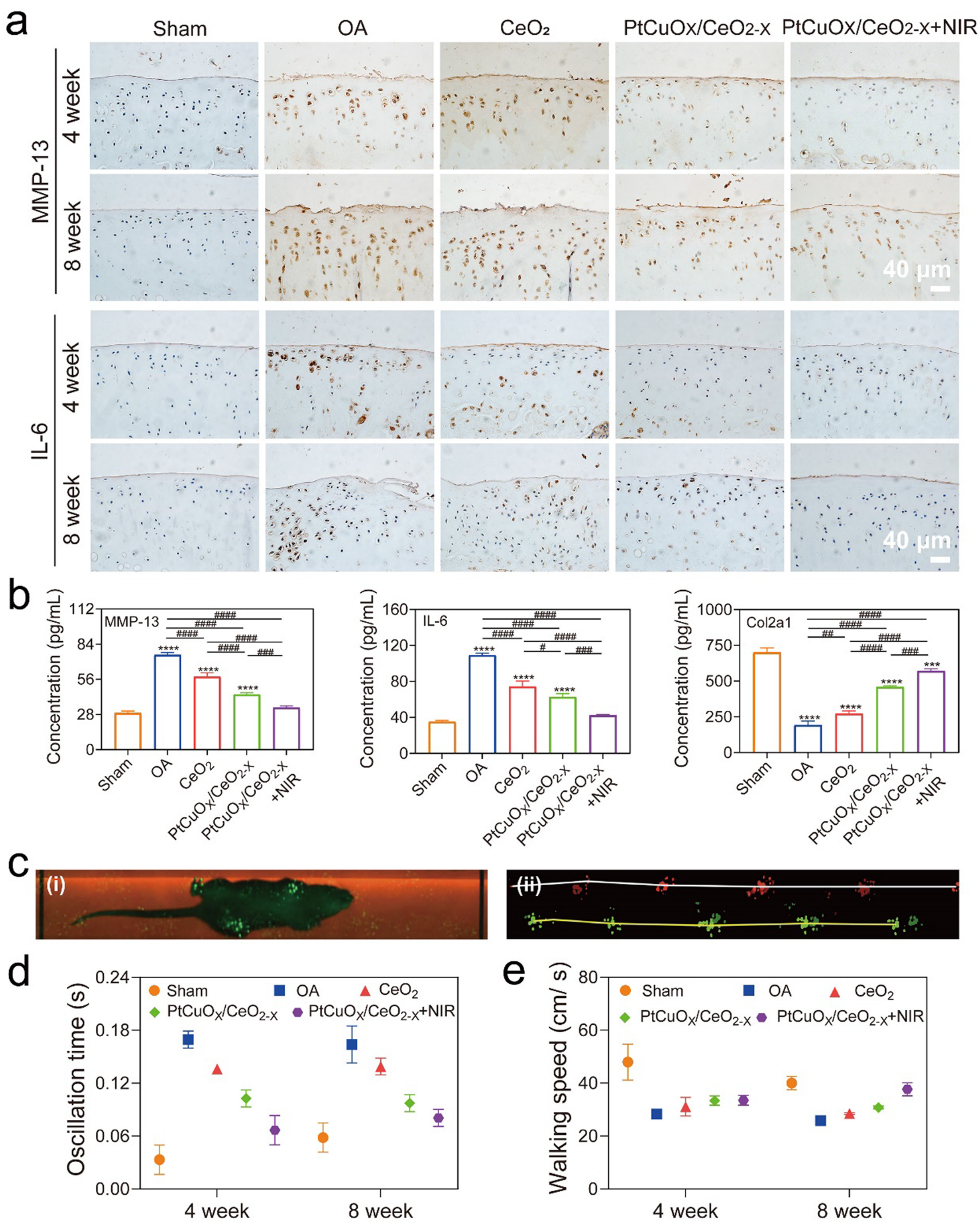

Fig. 8 In vivo treatment with $PtCuO_X/CeO_{2-X}$ nanozymes to inhibit inflammatory gene expression and attenuate OA. **a** IHC staining of the articular cartilage after 4 and 8 weeks of treatment. **b** Levels of inflammatory factors (MMP-13, IL-6) and chondrocyte-specific genes (Col2a1) in synovial fluid were determined using ELISA kits after 8 weeks of treatment. **c** Paw prints of rats walking on the CaitWalk platform. **d** Left hind paw swing time and **e** walking speed were measured using gait analysis after 4 and 8 weeks of treatment. Concentration: 50 μg/mL and 100 μL per injection, with injections once a week. NIR Parameters: Wavelength: 808 nm, Power: 1.0 W/cm^2, and Duration: 5 min. Data are expressed as mean ± SD (n = 3). * and # for P < 0.05, ** and ## for P < 0.01, *** and ### for P < 0.001, and **** and #### for P < 0.0001

nanozymes effectively scavenged intracellular ROS and RNS, protected mitochondrial function, and inhibited the inflammatory factors, thus reducing chondrocyte apoptosis. In vivo, experiments demonstrated the biosafety of $PtCuO_X/CeO_{2-X}$ and its potent effect on OA suppression. In particular, NIR radiation further enhanced the effects. Mechanistically, $PtCuO_X/CeO_{2-X}$ nanozymes reduced Rac-1 and *p*-p65 protein expression, and ROS levels to remodel the inflammatory microenvironment by inhibiting the ROS/Rac-1/NF-κB signaling pathway. This study is a promising strategy for the treatment of various ROS-mediated inflammatory diseases.

Supplementary Information

The online version contains supplementary material available at https://doi.org/10.1186/s12951-024-02678-z.

Supplementary file 1.

Acknowledgements
First-class discipline innovation-driven talent program of Guangxi Medical University

Author contributions
J.X.Y, S.H.X, and J.J.D contributed equally to this work. L.Z, Q.J.W, and J.P.Z conceived and designed this project. J.X.Y, S.H.X, J.J.D, Y.Q.L, H.H, J.W.W and G.H.L performed the experiments. J.X.Y, S.H.X, L.Z, Q.J.W, C.L, and J.P.Z analyzed and tackled the data. J.H.X, Y.Q.L, and J.P.Z re-arranged the Figures and wrote the manuscript. L.Z and J.P.Z revised the manuscript. L.Z, Q.J.W, and J.P.Z supervised and supported the project. All authors reviewed the manuscript.

Funding
This study was supported by the Guangxi Natural Science Foundation (2023GXNSFBA026020), the Guangxi Scientific Research and Technological Development Foundation (Grant No. GuikeAB23026049), National Natural Science Foundation of China (82160429, 52301303, 82360426), the Guangxi Key R&D Program, China (GuiKe AB22035014), Special Fund of Characteristic Innovation Team of the First Affiliated Hospital of Guangxi Medical University (YYZS2022003).

Data availability
The data that support the findings of this study are available from the corresponding author upon reasonable request.

Declarations

Ethics approval and consent to participate
All animal experiments met animal ethics requirements and were approved by the Ethics Committee of Guangxi Medical University. (No: 202209010).

Consent for publication
There is no conflict of interest in submitting this manuscript, and the manuscript is approved for publication by all authors.

Competing interests
The authors declare that they have no known competing financial interests or personal relationships that could have appeared to influence the work reported in this paper.

Author details
[1]Guangxi Engineering Center in Biomedical Material for Tissue and Organ Regeneration, Collaborative Innovation Centre of Regenerative Medicine and Medical BioResource Development and Application Co-Constructed By the Province and Ministry, Guangxi Key Laboratory of Regenerative Medicine, The First Affiliated Hospital of Guangxi Medical University, Guangxi Medical University, No. 6 Shuangyong Road, Nanning 530021, Guangxi, People's Republic of China. [2]Life Sciences Institute, Guangxi Medical University, No. 22 Shuangyong Road, Nanning, Guangxi 530021, People's Republic of China. [3]Department of Orthopaedics Trauma and Hand Surgery, The First Affiliated Hospital of Guangxi Medical University, No. 6 Shuangyong Road, Nanning, Guangxi 530021, People's Republic of China. [4]School of Materials and Environment, Guangxi Minzu University, Nanning, Guangxi 53000, People's Republic of China. [5]Department of Orthopedics, The Second Affiliated Hospital of Guangxi Medical University, No. 166 East University Road, Nanning, Guangxi 530005, People's Republic of China.

Received: 4 April 2024 Accepted: 30 June 2024
Published online: 18 August 2024

References
1. Leifer VP, Katz JN, Losina E. The burden of OA-health services and economics. Osteoarthritis Cartilage. 2022;30:10–6.
2. Bernabei I, So A, Busso N, Nasi S. Cartilage calcification in osteoarthritis: mechanisms and clinical relevance. Nat Rev Rheumatol. 2022;19:10–27.
3. Katz JN, Arant KR, Loeser RF. Diagnosis and treatment of hip and knee osteoarthritis. JAMA. 2021;325:568.
4. Arra M, Swarnkar G, Ke K, Otero JE, Ying J, Duan X, Maruyama T, Rai MF, O'Keefe RJ, Mbalaviele G, et al. LDHA-mediated ROS generation in chondrocytes is a potential therapeutic target for osteoarthritis. Nat Commun. 2020. https://doi.org/10.1038/s41467-020-17242-0.
5. Blanco FJ, Valdes AM, Rego-Pérez I. Mitochondrial DNA variation and the pathogenesis of osteoarthritis phenotypes. Nat Rev Rheumatol. 2018;14:327–40.
6. Shi S, Tian T, Li Y, Xiao D, Zhang T, Gong P, Lin Y. Tetrahedral framework nucleic acid inhibits chondrocyte apoptosis and oxidative stress through activation of autophagy. ACS Appl Mater Interfaces. 2020;12:56782–91.
7. Yang B, Chen Y, Shi J. Reactive oxygen species (ROS)-based nanomedicine. Chem Rev. 2019;119:4881–985.
8. Kwesiga MP, Gillette AA, Razaviamri F, Plank ME, Canull AL, Alesch Z, He W, Lee BP, Guillory RJ. Biodegradable magnesium materials regulate ROS-RNS balance in pro-inflammatory macrophage environment. Bioactive Mater. 2023;23:261–73.
9. Winand L, Sester A, Nett M. Bioengineering of anti-inflammatory natural products. Chem Med Chem. 2020;16:767–76.
10. Gu L, Shan T, Ma Y-X, Tay FR, Niu L. Novel biomedical applications of crosslinked collagen. Trends Biotechnol. 2019;37:464–91.
11. Arnold J, Chapman J, Arnold M, Dinu CZ. Hyaluronic acid allows enzyme immobilization for applications in biomedicine. Biosensors. 2022;12:28.
12. Wu J, Li S, Wei H. Multifunctional nanozymes: enzyme-like catalytic activity combined with magnetism and surface plasmon resonance. Nanoscale Horizons. 2018;3:367–82.
13. Wang H, Wan K, Shi X. Recent advances in nanozyme research. Adv Mater. 2018;31:e1805368.
14. Huang Y, Ren J, Qu X. Nanozymes: classification, catalytic mechanisms, activity regulation, and applications. Chem Rev. 2019;119:4357–412.
15. Saifi MA, Seal S, Godugu C. Nanoceria, the versatile nanoparticles: promising biomedical applications. J Control Release. 2021;338:164–89.
16. Gao Y, Zou J, Chen B, Cao Y, Hu D, Zhang Y, Zhao X, Wen J, Liu K, Wang K. Hyaluronic acid/serotonin-decorated cerium dioxide nanomedicine for targeted treatment of ulcerative colitis. Biomater Sci. 2023;11:618–29.
17. Lin Y-W, Fang C-H, Meng F-Q, Ke C-J, Lin F-H. Hyaluronic acid loaded with cerium oxide nanoparticles as antioxidant in hydrogen peroxide induced chondrocytes injury: an in vitro osteoarthritis model. Molecules. 2020;25:4407.
18. Zhang S, Ruan H, Xin Q, Mu X, Wang H, Zhang X-D. Modulation of the biocatalytic activity and selectivity of CeO2 nanozymes via atomic doping engineering. Nanoscale. 2023;15:4408–19.
19. Yang X, Pan H, Wang P, Zhao F-J. Particle-specific toxicity and bioavailability of cerium oxide (CeO2) nanoparticles to Arabidopsis thaliana. J Hazard Mater. 2017;322:292–300.
20. Zhang J, Qin X, Chu X, Chen M, Chen X, Chen J, He H, Zhang C. Tuning metal-support interaction of Pt-CeO2 catalysts for enhanced oxidation reactivity. Environ Sci Technol. 2021;55:16687–98.
21. Guo C, Wei S, Zhou S, Zhang T, Wang Z, Ng S-P, Lu X, Wu C-ML, Guo W. Initial reduction of CO2 on Pd-, Ru-, and Cu-doped CeO2(111) surfaces: effects of surface modification on catalytic activity and selectivity. ACS Appl Mater Interfaces. 2017;9:26107–17.
22. Zhang W, Pu M, Lei M. Theoretical studies on the stability and reactivity of the metal-doped CeO2(100) surface: toward H2 dissociation and oxygen vacancy formation. Langmuir. 2020;36:5891–901.

23. Zhang Z, Wang ZL, An K, Wang J, Zhang S, Song P, Bando Y, Yamauchi Y, Liu Y. Ti3+ tuning the ratio of Cu+/Cu0 in the ultrafine Cu nanoparticles for boosting the hydrogenation reaction. Small. 2021. https://doi.org/10.1002/smll.202008052.
24. Liu X, Jia S, Yang M, Tang Y, Wen Y, Chu S, Wang J, Shan B, Chen R. Activation of subnanometric Pt on Cu-modified CeO2 via redox-coupled atomic layer deposition for CO oxidation. Nat Commun. 2020. https://doi.org/10.1038/s41467-020-18076-6.
25. Zou L, Pan J, Xu F, Chen J. Cu assisted loading of Pt on CeO2 as a carbon-free catalyst for methanol and oxygen reduction reaction. RSC Adv. 2021;11:36726–33.
26. Zhu Y, Zhao R, Feng L, Wang C, Dong S, Zyuzin MV, Timin A, Hu N, Liu B, Yang P. Dual nanozyme-driven PtSn bimetallic nanoclusters for metal-enhanced tumor photothermal and catalytic therapy. ACS Nano. 2023;17:6833–48.
27. Yuan M, Kermanian M, Agarwal T, Yang Z, Yousefiasl S, Cheng Z, Pa M, Lin J, Maleki A. Defect engineering in biomedical sciences. Adv Mater. 2023;35:e2304176.
28. Jiang C, Wei X, Bao S, Tu H, Wang W. Cu@Au(Ag)/Pt nanocomposite as peroxidase mimic and application of Cu@Au/Pt in colorimetric detection of glucose and l-cysteine. RSC Adv. 2019;9:41561–8.
29. Xiong P, Niu H, Zhu Z, Zhao L, Zuo J, Gong S, Niu X, Chen JS, Wu R, Xia BY. Engineering a high-loading Sub-4 nm intermetallic platinum-cobalt alloy on atomically dispersed cobalt-nitrogen-carbon for efficient oxygen reduction in fuel cells. Nano Lett. 2024;24:3961–70.
30. Zhong J-P, Hou C, Li L, Waqas M, Fan Y-J, Shen X-C, Chen W, Wan L-Y, Liao H-G, Sun S-G. A novel strategy for synthesizing Fe, N, and S tri doped graphene-supported Pt nano dendrites toward highly efficient methanol oxidation. J Catal. 2020;381:275–84.
31. Kresse G, Furthmüller J. Efficient iterative schemes for ab initio total-energy calculations using a plane-wave basis set. Phys Rev B Condens Matter. 1996;54:11169–86.
32. Perdew JP, Burke K, Ernzerhof M. Generalized Gradient Approximation Made Simple. Phys Rev Lett. 1996;77:3865–8.
33. Sun Y, Liu X, Wang L, Xu L, Liu K, Xu L, Shi F, Zhang Y, Gu N, Xiong F. High-performance SOD mimetic enzyme Au@Ce for arresting cell cycle and proliferation of acute myeloid leukemia. Bioactive Mater. 2022;10:117–30.
34. Yang L, Cai Z, Hao L, Xing Z, Dai Y, Xu X, Pan S, Duan Y, Zou J. Nano Ce2O2S with highly enriched oxygen-deficient Ce3+ sites supported by N and S dual-doped carbon as an active oxygen-supply catalyst for the oxygen reduction reaction. ACS Appl Mater Interfaces. 2017;9:22518–29.
35. Sun X, Yang S, Liu X, Qiao Y, Liu Z, Li X, Pan J, Liu H, Wang L. The enhancement of benzene total oxidation over RuxCeO2 catalysts at low temperature: the significance of Ru incorporation. Sci Total Environ. 2023;902:165574.
36. Wang Z, Shen X, Gao X, Zhao Y. Simultaneous enzyme mimicking and chemical reduction mechanisms for nanoceria as a bio-antioxidant: a catalytic model bridging computations and experiments for nanozymes. Nanoscale. 2019;11:13289–99.
37. Xu C, Zhang W, Wang R, Tan S, Holub JM, Tang B. Versatile gold-coupled Te-carbon dots for quantitative monitoring and efficient scavenging of superoxide anions. Anal Chem. 2021;93:9111–8.
38. Yu P, Li Y, Sun H, Zhang H, Kang H, Wang P, Xin Q, Ding C, Xie J, Li J. Mimicking antioxidases and hyaluronan synthase: a zwitterionic nanozyme for photothermal therapy of osteoarthritis. Adv Mater. 2023. https://doi.org/10.1002/adma.202303299.
39. Largo R, Alvarez-Soria MA, Dıez-Ortego I, Calvo E, Sánchez-Pernaute O, Egido J, Herrero-Beaumont G. Glucosamine inhibits IL-1β-induced NFκB activation in human osteoarthritic chondrocytes. Osteoarthritis Cartil. 2003;11:290–8.
40. Paggio A, Checchetto V, Campo A, Menabò R, Di Marco G, Di Lisa F, Szabo I, Rizzuto R, De Stefani D. Identification of an ATP-sensitive potassium channel in mitochondria. Nature. 2019;572:609–13.
41. King LE, Rodriguez-Enriquez R, Pedley R, Mellor CEL, Wang P, Zindy E, White MRH, Brennan K, Gilmore AP. Apoptotic priming is defined by the dynamic exchange of Bcl-2 proteins between mitochondria and cytosol. Cell Death Differ. 2022;29:2262–74.
42. Huang Q, Li F, Liu X, Li W, Shi W, Liu F-F, O'Sullivan B, He Z, Peng Y, Tan A-C, et al. Caspase 3–mediated stimulation of tumor cell repopulation during cancer radiotherapy. Nat Med. 2011;17:860–6.
43. Bernardini JP, Brouwer JM, Tan IKL, Sandow JJ, Huang S, Stafford CA, Bankovacki A, Riffkin CD, Wardak AZ, Czabotar PE, et al. Parkin inhibits BAK and BAX apoptotic function by distinct mechanisms during mitophagy. EMBO J. 2018. https://doi.org/10.15252/embj.201899916.
44. Zheng L, Zhang Z, Sheng P, Mobasheri A. The role of metabolism in chondrocyte dysfunction and the progression of osteoarthritis. Ageing Res Rev. 2021;66:101249.
45. He R, Wang Z, Cui M, Liu S, Wu W, Chen M, Wu Y, Qu Y, Lin H, Chen S, et al. HIF1A Alleviates compression-induced apoptosis of nucleus pulposus derived stem cells via upregulating autophagy. Autophagy. 2021;17:3338–60.
46. Lan Q, Lu R, Chen H, Pang Y, Xiong F, Shen C, Qin Z, Zheng L, Xu G, Zhao J. MMP-13 enzyme and pH-responsive theranostic nano platform for osteoarthritis. J Nanobiotechnol. 2020. https://doi.org/10.1186/s12951-020-00666-7.
47. Del Giudice M, Gangestad SW. Rethinking IL-6 and CRP: why they are more than inflammatory biomarkers, and why it matters. Brain Behav Immun. 2018;70:61–75.
48. Giuliani C. The flavonoid quercetin induces AP-1 activation in FRTL-5 thyroid cells. Antioxidants. 2019. https://doi.org/10.3390/antiox8050112.
49. Qian H, Neplioueva V, Shetty GA, Channon KM, George SE. Nitric Oxide Synthase Gene Therapy Rapidly Reduces Adhesion Molecule Expression and Inflammatory Cell Infiltration in Carotid Arteries of Cholesterol-Fed Rabbits. Circulation. 1999;99:2979–82.
50. Kapoor M, Martel-Pelletier J, Lajeunesse D, Pelletier J-P, Fahmi H. Role of proinflammatory cytokines in the pathophysiology of osteoarthritis. Nat Rev Rheumatol. 2010;7:33–42.
51. Hou W, Ye C, Chen M, Gao W, Xie X, Wu J, Zhang K, Zhang W, Zheng Y, Cai X. Excavating bioactivities of nanozyme to remodel microenvironment for protecting chondrocytes and delaying osteoarthritis. Bioactive Materials. 2021;6:2439–51.
52. Zhu S, Dai J, Liu H, Cong X, Chen Y, Wu Y, Hu H, Heng BC, Ouyang HW, Zhou Y. Down-regulation of Rac GTPase-activating protein OCRL1 causes aberrant activation of Rac1 in osteoarthritis development. Arthritis Rheumatol. 2015;67:2154–63.
53. Yao Q, Wu X, Tao C, Gong W, Chen M, Qu M, Zhong Y, He T, Chen S, Xiao G. Osteoarthritis: pathogenic signaling pathways and therapeutic targets. Signal Transduction Targeted Ther. 2023. https://doi.org/10.1038/s41392-023-01330-w.
54. Myant Kevin B, Cammareri P, McGhee Ewan J, Ridgway Rachel A, Huels David J, Cordero Julia B, Schwitalla S, Kalna G, Ogg E-L, Athineos D, et al. ROS production and NF-κB activation triggered by RAC1 facilitate WNT-driven intestinal stem cell proliferation and colorectal cancer initiation. Cell Stem Cell. 2013;12:761–73.
55. Turpaev KT. Transcription Factor KLF2 and Its role in the regulation of inflammatory processes. Biochemistry. 2020;85:54–67.
56. Glasson SS, Blanchet TJ, Morris EA. The surgical destabilization of the medial meniscus (DMM) model of osteoarthritis in the 129/SvEv mouse. Osteoarthritis Cartilage. 2007;15:1061–9.
57. Pelletier JP, Fernandes JC, Brunet J, Moldovan F, Schrier D, Flory C, Martel-Pelletier J. In vivo selective inhibition of mitogen-activated protein kinase 1/2 in rabbit experimental osteoarthritis is associated with a reduction in the development of structural changes. Arthritis Rheum. 2003;48:1582–93.
58. Pritzker KPH, Gay S, Jimenez SA, Ostergaard K, Pelletier JP, Revell PA, Salter D, van den Berg WB. Osteoarthritis cartilage histopathology: grading and staging. Osteoarthritis Cartilage. 2006;14:13–29.
59. Chen Q, Chen J, Yang Z, Xu J, Xu L, Liang C, Han X, Liu Z. Nanoparticle-enhanced radiotherapy to trigger robust cancer immunotherapy. Adv Mater. 2019;31:e1802228.

Publisher's Note